Article

Cell

A Distinct Gene Module for Dysfunction Uncoupled from Activation in Tumor-Infiltrating T Cells

Graphical Abstract

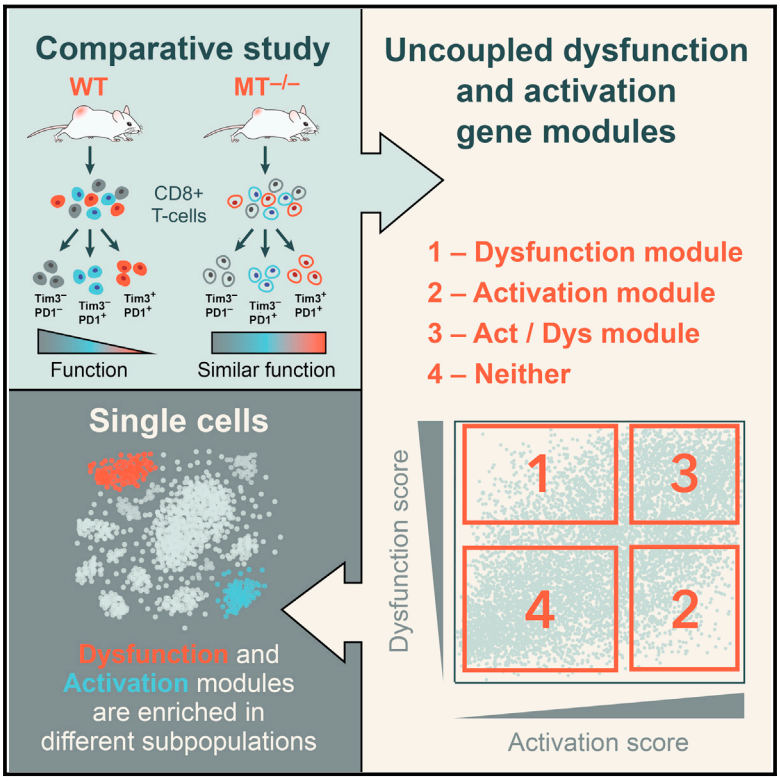

Authors

Meromit Singer, Chao Wang, Le Cong, ..., Vijay K. Kuchroo, Aviv Regev, Ana C. Anderson

Correspondence

vkuchroo@evergrande.hms.harvard.edu (V.K.K.), aregev@broadinstitute.org (A.R.), acanderson@partners.org (A.C.A.)

In Brief

Single-cell profiling of tumor-infiltrating lymphocytes identifies critical regulators of T cell dysfunction in cancer, opening new avenues for targeting dysfunctional T cell states while leaving activation programs intact.

Highlights

- Distinct gene modules for T cell dysfunction and activation can be uncoupled
- Single-cell profiling of CD8 TILs shows that these modules are exclusive
- Metallothioneins, zinc regulators, promote T cell dysfunction
- CRISPR-Cas9 targeting shows Gata-3, a zinc-finger TF, promotes dysfunction

Data Resources

GSE86042

Singer et al., 2016, Cell *166*, 1500–1511
September 8, 2016
http://dx.doi.org/10.1016/j.cell.2016.08.052

CellPress

Cell

Article

A Distinct Gene Module for Dysfunction Uncoupled from Activation in Tumor-Infiltrating T Cells

Meromit Singer,[1,6] Chao Wang,[2,6] Le Cong,[1] Nemanja D. Marjanovic,[1,3] Monika S. Kowalczyk,[1] Huiyuan Zhang,[2] Jackson Nyman,[1] Kaori Sakuishi,[2] Sema Kurtulus,[2] David Gennert,[1] Junrong Xia,[2] John Y.H. Kwon,[1] James Nevin,[2] Rebecca H. Herbst,[1] Itai Yanai,[4] Orit Rozenblatt-Rosen,[1] Vijay K. Kuchroo,[2,*] Aviv Regev,[1,3,5,*] and Ana C. Anderson[2,7,*]

[1]Broad Institute of MIT and Harvard, Cambridge, MA 02142, USA

[2]Evergrande Center for Immunologic Diseases and Ann Romney Center for Neurologic Diseases, Harvard Medical School and Brigham and Women's Hospital, Boston, MA 02115, USA

[3]Department of Biology, Koch Institute and Ludwig Center, Massachusetts Institute of Technology, Cambridge, MA 02142, USA

[4]Institute for Computational Medicine and Department of Biochemistry and Molecular Pharmacology, New York University School of Medicine, New York, NY 10016, USA

[5]Howard Hughes Medical Institute, Chevy Chase, MD 20815, USA

[6]Co-first author

[7]Lead Contact

*Correspondence: vkuchroo@evergrande.hms.harvard.edu (V.K.K.), aregev@broadinstitute.org (A.R.), acanderson@partners.org (A.C.A.)

http://dx.doi.org/10.1016/j.cell.2016.08.052

SUMMARY

Reversing the dysfunctional T cell state that arises in cancer and chronic viral infections is the focus of therapeutic interventions; however, current therapies are effective in only some patients and some tumor types. To gain a deeper molecular understanding of the dysfunctional T cell state, we analyzed population and single-cell RNA profiles of CD8$^+$ tumor-infiltrating lymphocytes (TILs) and used genetic perturbations to identify a distinct gene module for T cell dysfunction that can be uncoupled from T cell activation. This distinct dysfunction module is downstream of intracellular metallothioneins that regulate zinc metabolism and can be identified at single-cell resolution. We further identify Gata-3, a zinc-finger transcription factor in the dysfunctional module, as a regulator of dysfunction, and we use CRISPR-Cas9 genome editing to show that it drives a dysfunctional phenotype in CD8$^+$ TILs. Our results open novel avenues for targeting dysfunctional T cell states while leaving activation programs intact.

INTRODUCTION

During persistent immune activation, such as uncontrolled tumor growth or chronic viral infections, the ability of CD8$^+$ lymphocytes to secrete pro-inflammatory cytokines and elaborate cytotoxic function becomes compromised to different extents (Anderson et al., 2016; Baitsch et al., 2012; Kim and Ahmed, 2010; Wherry and Kurachi, 2015; Zuniga et al., 2015). Such dysfunctional, or "exhausted," CD8$^+$ cells are believed to constitute a barrier to successful anti-tumor and anti-viral immunity. Gaining a clear molecular understanding of the dysfunctional T cell state can thus help develop successful therapeutic interventions.

Dysfunctional CD8$^+$ T cells from LCMV-infected mice (Blackburn et al., 2009; Wherry et al., 2007) and cancer (Baitsch et al., 2011; Fourcade et al., 2010; Matsuzaki et al., 2010; Sakuishi et al., 2010) differ profoundly from memory CD8$^+$ T cells and co-express multiple co-inhibitory or immune checkpoint receptors such as PD-1, Lag-3, and Tim-3. Indeed, therapeutic targeting of co-inhibitory receptors, such as CTLA-4 and PD-1, with blocking antibodies has achieved great success in cancer patients. However, many patients still fail to respond, and some cancers are refractory to these therapies (Restifo et al., 2016). Thus, to identify novel therapeutic targets and stratify patients, it is important to better understand the dysfunctional T cell state.

A major challenge to developing therapies that specifically target the dysfunctional CD8$^+$ T cell state is that current markers and transcriptional signatures of dysfunction are closely intertwined with the activated CD8$^+$ T cell state (Doering et al., 2012; Fuertes Marraco et al., 2015; Tirosh et al., 2016). This is not surprising, given that T cell dysfunction arises in the face of chronic T cell activation. Thus, both dysfunctional CD8$^+$ T cells and activated CD8$^+$ T cells upregulate genes involved in activation of the cell cycle, T cell homing, and migration, as well as effector molecules, such as granzymes and co-stimulatory and co-inhibitory receptors that mark T cells for subsequent regulation (Giordano et al., 2015; Wherry et al., 2007). Moreover, both cell types downregulate memory cell gene signatures (Doering et al., 2012; Wherry et al., 2007). Indeed, T cell dysfunction likely evolved as a physiological process to balance T cell activation with self-regulation in the face of chronic antigen persistence, thereby limiting immunopathology. As a result, it has been challenging to identify markers and approaches that would specifically target the dysfunctional T cell state while preserving the activated T cell state, as well as to identify bona fide dysfunctional T cells in vivo.

Here, we used an integrated experimental and computational approach to systematically dissect the molecular pathways associated with activation and dysfunction within CD8$^+$ tumor-infiltrating lymphocytes (TILs). We find that metallothioneins,

intracellular zinc chaperones, are highly enriched in the most dysfunctional CD8$^+$ TILs and demonstrate that targeted deletion of metallothioneins results in loss of T cell dysfunction and significantly reduced tumor growth despite no reduction in the expression of co-inhibitory molecules. We analyzed metallothionein-deficient CD8$^+$ TILs and identified a novel dysfunction gene module that is distinct from that of T cell activation. Using single-cell RNA sequencing (RNA-seq), we show that the activation and dysfunction gene modules are mutually exclusive at the single-cell level and that cells primarily expressing the dysfunction module are absent among metallothionein-deficient CD8$^+$ TILs. We further use CRISPR-Cas9 genome editing of primary T cells to demonstrate that one of the major predicted regulators of the dysfunction module, the zinc-finger transcription factor Gata-3, is a key driver of T cell dysfunction in CD8$^+$ T cells in cancer. Our analysis identifies a gene module that is expressed in dysfunctional T cells, but not in activated T cells, and defines critical molecular nodes that control this module, opening the way to develop targeted therapy specific for the dysfunctional T cell state.

RESULTS AND DISCUSSION

Transcriptional Signatures for CD8$^+$ T Cell Dysfunction and Activation Are Intertwined

CD8$^+$ TILs exhibit distinct functional phenotypes that we (Sakuishi et al., 2010) and others (Baitsch et al., 2011; Fourcade et al., 2010; Matsuzaki et al., 2010; Zhou et al., 2011) have previously defined using a combination of co-inhibitory receptors as markers. Specifically, cell surface expression of T cell immunoglobulin and mucin-domain-containing-3 (Tim-3) and programmed cell death-1 (PD-1) can be used to partition CD8$^+$ TILs into three different groups: Tim-3$^-$PD-1$^-$ (DN, double negative), Tim-3$^-$PD-1$^+$ (SP, single positive), and Tim-3$^+$PD-1$^+$ (DP, double positive). DN TILs exhibit full effector function, SP TILs exhibit partial dysfunction, and DP TILs exhibit severe dysfunction, as reflected by the respective differences in their ability to produce effector cytokines (Sakuishi et al., 2010).

To study the molecular programs associated with the functional spectrum of CD8$^+$ TILs, we measured the transcriptional profiles of CD8$^+$ DN, SP, and DP TILs (Figure 1A and STAR Methods) (Johnson et al., 2007; Reich et al., 2006; Subramanian et al., 2005). We did not examine CD8$^+$ Tim-3$^+$PD1$^-$ TILs, because these cells are rarely observed in growing tumors. For comparison, we profiled CD8$^+$ CD44^{hi}CD62^{Low} effector/memory (EffMem) and naive CD8$^+$ CD44^{low}CD62L^{high} T cells from non-tumor-bearing mice. We identified 3,031 genes that were differentially expressed (STAR Methods and Table S1) across the three TIL subpopulations (Figure 1B). The gene-expression profiles of DP and SP TILs were similar to each other, while the profile of DN TILs was distinct and shared some features with both naive and EffMem CD8$^+$ T cells (Figure 1B).

We identified ten clusters (*k*-means clustering; C1–C10, STAR Methods) with distinct gene expression patterns across the cell populations (Figures 1B and S1). Some of these clusters showed either gradual increase or gradual decrease from DN to SP to DP TILs, suggesting a possible association with the functional differences observed in these populations. Of the ten clusters, only cluster 2 (C2) was significantly enriched for genes upregulated in a viral CD8$^+$ T cell exhaustion signature (Doering et al., 2012) (Figure 1C, $p < 0.0002$, hypergeometric test). However, cluster 2 was also strongly enriched ($p < 10^{-5}$) for genes upregulated in an in vivo CD8$^+$ T cell activation signature (Sarkar et al., 2008) (Figure 1C). Conversely, clusters 3 and 4 were enriched for genes highly expressed in naive T cells (Figure 1B, $p < 0.004$, 10^{-5}, respectively, Table S2).

The transcriptional coupling of T cell activation and dysfunction has been observed previously (Doering et al., 2012; Tirosh et al., 2016) and is not surprising given that T cell dysfunction/exhaustion arises from chronic T cell activation due to antigen persistence. This, however, raises the fundamental question of whether a distinct gene module for T cell dysfunction exists and, if so, whether it is exclusively expressed by a subset of CD8$^+$ TILs. We hypothesized that characterizing CD8$^+$ TILs following perturbations of the dysfunctional state might allow us to refine the dysfunction signature. We therefore focused on the members of cluster 2. Ranking cluster 2 genes by their differential expression across the three TIL subpopulations, we identified metallothionein 1 (MT1) as the top-ranking gene in this cluster (Figure 1D and Table S1).

Metallothionein Deficiency Affects Tumor Growth in a T-Cell-Intrinsic Manner

Metallothioneins are cysteine-rich intracellular proteins with high affinity for zinc that serve as zinc chaperones and regulate zinc metabolism. Consequently, metallothioneins can impact immune responses through actions on diverse zinc-dependent proteins, including zinc-finger transcription factors and kinases (Bonaventura et al., 2015; Hamer, 1986). We confirmed that both MT1 and its co-regulated paralog MT2 are consistently upregulated in highly dysfunctional CD8$^+$ DP TILs in two different mouse tumor models (Figure S2A). Given the role of MT1 and MT2 in zinc regulation, we further examined whether zinc availability is modulated in these TILs populations and found that the availability of intracellular zinc closely parallels the upregulation of MT1 and MT2 in DP CD8$^+$ TILs (Figure S2B). Thus, the expression of MT1 and MT2 and elevated zinc status correlate with loss of effector function and acquisition of a dysfunctional phenotype. We therefore hypothesized that MT1 and MT2 may regulate CD8$^+$ T cell dysfunction and impact anti-tumor immunity.

To examine the role of MT1 and MT2 in regulating T cell dysfunction and tumor growth, we investigated the effect of MT1 and MT2 deficiency using knockout mice. There was a significant delay in the growth of B16F10 melanoma in mice deficient in both MT1 and MT2 ($MT^{-/-}$) compared to littermate controls (Figure 2A). Furthermore, CD8$^+$ T cells isolated from the tumors and tumor-draining lymph nodes of $MT^{-/-}$ mice exhibited increased proliferation in response to stimulation with tumor-specific antigen, indicating an improved anti-tumor CD8$^+$ T cell response (Figure 2B). MT1 and MT2 deficiency also reversed the increased zinc observed in DP CD8$^+$ TILs (Figure S2B). To confirm a T cell intrinsic role of metallothioneins in regulating anti-tumor responses, we used a system in which adoptive transfer of Ova-specific OT1 CD8$^+$ T cells to mice bearing MC38 tumors that express Ova (MCA38-Ova) shows tumor growth control. We overexpressed MT1 in OT1 CD8$^+$

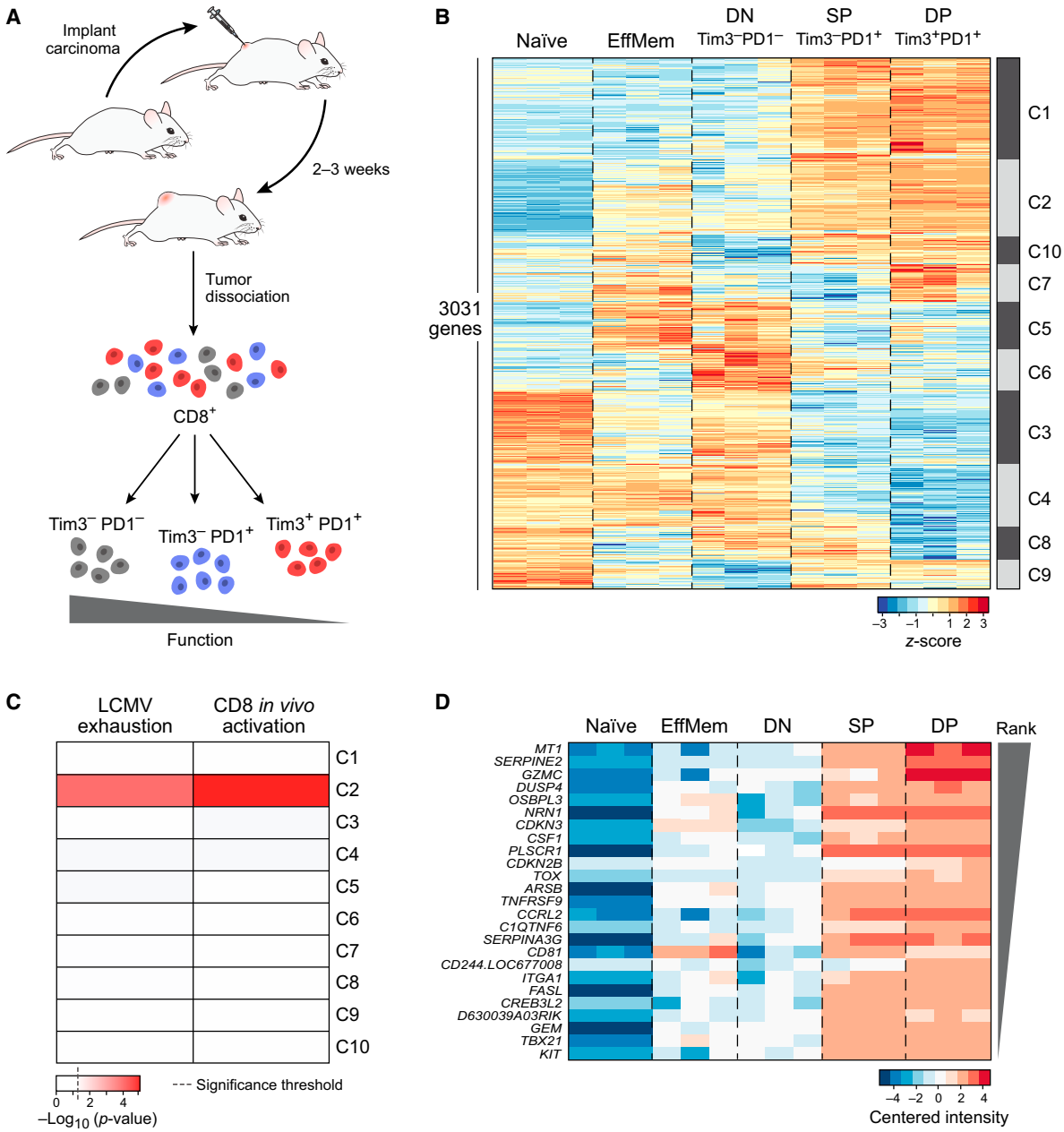

Figure 1. CD8$^+$ T Cell Dysfunction and Activation Are Transcriptionally Intertwined

(A) Outline of experimental strategy. CT26 colon carcinoma was used.

(B) Heatmap of the 3,031 differentially expressed genes across the TIL subpopulations. Naive: CD8$^+$CD62L^{hi}CD44^{low} cells from non-tumor-bearing Balb/c mice; EffMem: effector memory CD8$^+$CD62L^{low}CD44^{hi} cells from non-tumor-bearing Balb/c mice; DN: CD8$^+$Tim3$^-$PD1$^-$; SP: CD8$^+$Tim3$^-$PD1$^+$; DP: CD8$^+$Tim3$^+$PD1$^+$ TILs from CT26 colon carcinoma.

(C) Cluster 2 is significantly enriched with genes upregulated in a CD8$^+$ viral exhaustion signature (Doering et al., 2012), as well as an in vivo CD8$^+$ activation signature (Sarkar et al., 2008). p values determined by hypergeometric test.

(D) Heatmap of the top-ranking genes from cluster 2.

See also Figure S1 and Tables S1 and S2.

T cells and transferred these cells or control OT-1 CD8$^+$ T cells into wild-type (WT) mice bearing MC38-Ova tumors. Recipients of MT-OT1 CD8$^+$ T cells failed to exhibit tumor growth control compared to recipients of control OT-1 CD8$^+$ T cells (Figure 2C). Indeed, tumor growth in recipients of MT-OT1 CD8$^+$ T cells resembled that of mice that did not receive any tumor-antigen-specific CD8$^+$ T cells. These results indicate a CD8$^+$ T cell intrinsic role of MT. Taken together, our data support that expression of metallothioneins in CD8$^+$ T cells plays a critical role in suppressing anti-tumor CD8$^+$ T cell responses.

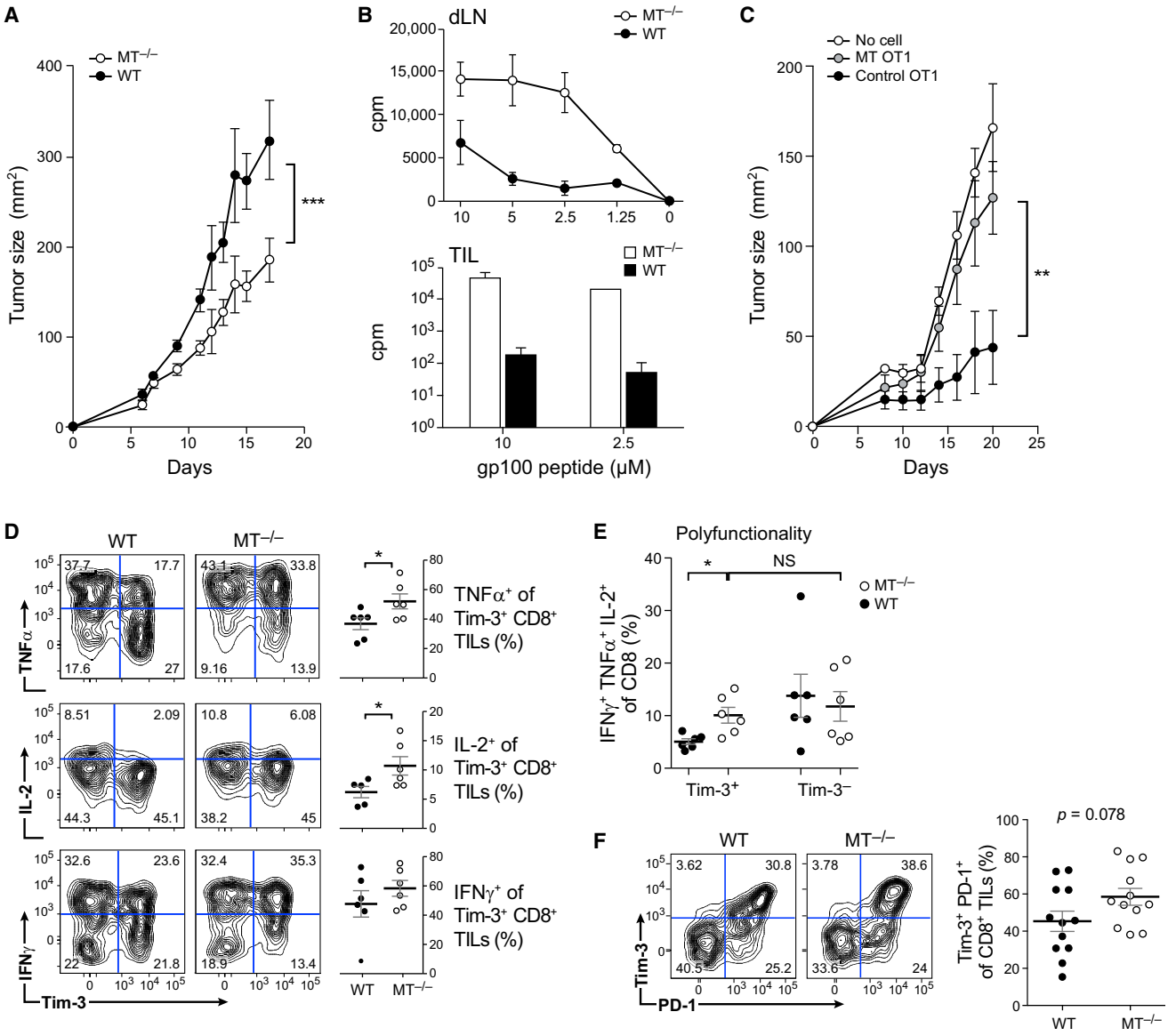

Figure 2. Metallothionein Deficiency Improves Anti-tumor Immunity and Reverses T Cell Dysfunction

(A and B) Mice deficient in both MT1 and MT2 ($MT^{-/-}$) and WT littermate controls were implanted subcutaneously with B16F10 melanoma. (A) Mean tumor growth. Statistical analysis was performed using linear regression ***$p < 0.001$. (B) Tumor-draining lymph node (dLN, top) and tumor-infiltrating lymphocytes (TIL, bottom) were isolated from WT and $MT^{-/-}$ mice 15 days post-tumor inoculation and stimulated with tumor antigen gp100. On day 3, tumor-antigen-specific proliferation was measured by ^{3}H incorporation.

(C) Naive OT-1 cells were sorted, activated, and infected with empty retrovirus (control OT1) or MT1 retrovirus (MT OT1) prior to transfer (1×10^{6} cells/mouse) into WT mice that were subsequently implanted with MC38-OVA tumor the next day. Mean tumor growth is shown. Statistical analysis was performed using linear regression. **$p < 0.01$.

(D and E) $MT^{-/-}$ $CD8^{+}$ TILs have increased functionality as compared to WT $CD8^{+}$ TILs. TILs were isolated and stimulated with PMA/ionomycin in the presence of brefeldin A for 4 hr prior to extracellular and intracellular staining and analysis by flow cytometry. *$p < 0.05$.

(F) Tim-3 and PD-1 expression in WT and $MT^{-/-}$ TILs. The DN, SP, and DP subpopulations are present in both the WT and $MT^{-/-}$ TILs.

See also Figure S2.

Metallothionein Deficiency Uncouples Co-inhibitory Receptor Expression from a T Cell Dysfunction Phenotype

We next analyzed the functional phenotype of $CD8^{+}$ TILs isolated from WT and $MT^{-/-}$ tumor-bearing mice. Consistent with retarded tumor growth, the effector function of $MT^{-/-}$ $CD8^{+}$ $Tim\text{-}3^{+}$ TILs was significantly improved, with higher production of interleukin-2 (IL-2), tumor necrosis factor α (TNF-α), and granzyme B (Figures 2D and S2C) and a higher percentage of polyfunctional T cells (Figure 2E). However, despite the enhanced

effector function and retarded tumor growth in $MT^{-/-}$ mice, Tim-3 and PD-1 expression was either unchanged or even increased on $MT^{-/-}$ $CD8^+$ TILs (Figure 2F) such that, in the setting of metallothionein deficiency, Tim3 and PD-1 expression is no longer associated with a dysfunctional T cell phenotype but, rather, with an activated T cell phenotype. This uncoupling of co-inhibitory receptor expression from a dysfunctional T cell phenotype suggested that co-inhibitory receptors may be part of a transcriptional program that is associated with T cell activation and is separable from the transcriptional program that drives dysfunction in $CD8^+$ T cells.

Expression Profiling of $MT^{-/-}$ TILs Identifies Distinct Programs for T Cell Activation and T Cell Dysfunction

To identify putative gene programs that are distinctly associated with T cell dysfunction, we leveraged our observation that the dysfunctional phenotype of WT $Tim3^+PD\text{-}1^+$ $CD8^+$ TILs is absent in $MT^{-/-}$ $Tim3^+PD\text{-}1^+$ TILs (Figures 2D–2F). We hypothesized that comparing transcriptional profiles between the dysfunctional (WT) and activated ($MT^{-/-}$) $CD8^+$ TIL populations could identify gene modules and pathways that are specific to the dysfunctional phenotype. We surmised that, while both programs should be co-expressed in the $CD8^+$ $Tim3^+PD1^+$ population in dysfunctional (WT) cells, any modules related to the dysfunction phenotype per se should be absent from the functional ($MT^{-/-}$) cells. We therefore profiled the $CD8^+$ DN, SP, and DP TIL populations from both WT and $MT^{-/-}$ tumor-bearing mice and then performed unsupervised principle component analysis (PCA) of the samples using the 4,155 genes that were both highly expressed and variable across the $CD8^+$ TIL subsets (Figures 3A and 3B, STAR Methods) (Langmead et al., 2009; Li and Dewey, 2011; Picelli et al., 2013).

The first principle component (PC1; 38% of variance) distinguished the DN, SP, and DP populations of $CD8^+$ TILs similarly for WT and $MT^{-/-}$ mice and in a manner reflecting their transcriptional activation status (Figure 3B, x axis; black, blue, red, respectively). In both WT and $MT^{-/-}$, the DN, SP, and DP profiles had respectively increasing scores on PC1, with DP populations scoring highest (Figure 3C). $MT^{-/-}$ DPs scored higher than WT DPs and had the strongest association with PC1. Thus, we inferred that PC1 separated cells based on their activation status, with high activation associated with high PC1 scores. Indeed, cell-cycle-associated signatures were highly enriched for the PC1 loadings ($p < 10^{-3}$, GSEA pre-ranked test, Table S3); a signature for $CD8^+$ in vivo activation (Sarkar et al., 2008) was positively correlated with PC1 (Figure 3E and STAR Methods); and naive and in-vitro-activated $CD8^+$ T cells isolated from non-tumor-bearing WT mice had low and high PC1 scores, respectively (Figure S3). Interestingly, previously annotated signatures of T cell dysfunction/exhaustion (Doering et al., 2012) and our cluster 2 gene signature (Figure 1D) were also positively correlated with PC1 (Figure 3E), consistent with the coupling between activation and dysfunction/exhaustion. Collectively, these data indicate that PC1 captures a transcriptional signature for $CD8^+$ T cell activation and that the enrichment of previously annotated T cell exhaustion signatures with PC1 genes likely reflects the coupling of the T cell activation and dysfunction gene modules.

Conversely, while PC2 (8.4% of variance) clearly distinguished the DN, SP, and DP $CD8^+$ TIL populations from WT mice, it did not distinguish between these populations from $MT^{-/-}$ mice (Figure 3D) and did not separate naive and in-vitro-activated T cells (Figure S3). Since T cell dysfunction is observed in WT, but not in $MT^{-/-}$, $CD8^+$ TILs, we hypothesized that PC2 and its associated genes could contribute to the uniquely dysfunctional phenotype in WT $CD8^+$ TILs. Interestingly, PC2 genes had no significant association with known signatures of T cell activation, with previously annotated signatures of T cell dysfunction/exhaustion, or with other features of T cell biology (Table S3). Thus, our analysis shows that, while the WT TIL populations have independent contributions from both PC1 and PC2 (Figures 3C and 3D), previously annotated signatures of T cell dysfunction only account for the separation observed on PC1.

A Novel Signature for T Cell Dysfunction

We leveraged the uncoupling of T cell activation from T cell dysfunction to annotate a novel and distinct signature for T cell dysfunction. To this end, we generated two scores for each gene: one for its association with activation and the other for dysfunction. Since only WT TILs exhibit dysfunction, as reflected on PC2, we computed the "dysfunction score" only from the WT subpopulation samples. Each gene's dysfunction score was defined as (−1) times the Pearson correlation coefficient between the gene's expression profile across the WT samples and those samples' PC2 scores (Figure 4A, y axis). Since the $MT^{-/-}$ TILs have the least dysfunction and separate best on PC1 (Figure 3C), we computed an "activation score" for each gene to be the Pearson correlation coefficient between a gene's expression profile across the $MT^{-/-}$ samples and those samples' PC1 scores (Figure 4A, x axis). Finally, we ranked the genes with respect to the four corners of the plot by projecting each gene onto each of the two diagonals to identify genes associated with dysfunction, but not activation (upper-left corner); activation, but not dysfunction (lower-right corner); both activation and dysfunction (upper-right corner); and neither (lower-left corner) (Figure 4A, marked "1", "2", "3", and "4", respectively). Finally, we generated gene signatures for each of these four modules (STAR Methods and Table S4).

As expected, the activation/dysfunction module had high scores for genes previously associated with T cell dysfunction such as co-inhibitory receptors (e.g., PD-1, Tim-3, TIGIT, and CTLA-4). Interestingly, we also observed high scores for several co-stimulatory receptors of the TNF receptor family, including TNFRSF9 (4-1BB), TNFRSF4 (OX-40), and TNFRSF18 (GITR) (Figure 4B). The presence of TNF receptor family co-stimulatory receptors together with co-inhibitory receptors in this module could reflect shared regulatory mechanisms for these receptors.

Furthermore, each of the four modules was significantly associated with distinct signatures (mHG ranked test; Figure 4C). As expected, the activation/dysfunction module was enriched for signatures of $CD8^+$ T cell activation in vivo (Sarkar et al., 2008) and in vitro (STAR Methods), as well as for previously annotated signatures for T cell dysfunction (Doering et al., 2012) and our cluster 2 gene signature (Figure 1D). The activation module was most significantly associated with the signature for in vitro activation (Figure 4C). The module with neither high activation nor high dysfunction scores was enriched for naive $CD8^+$ T cell

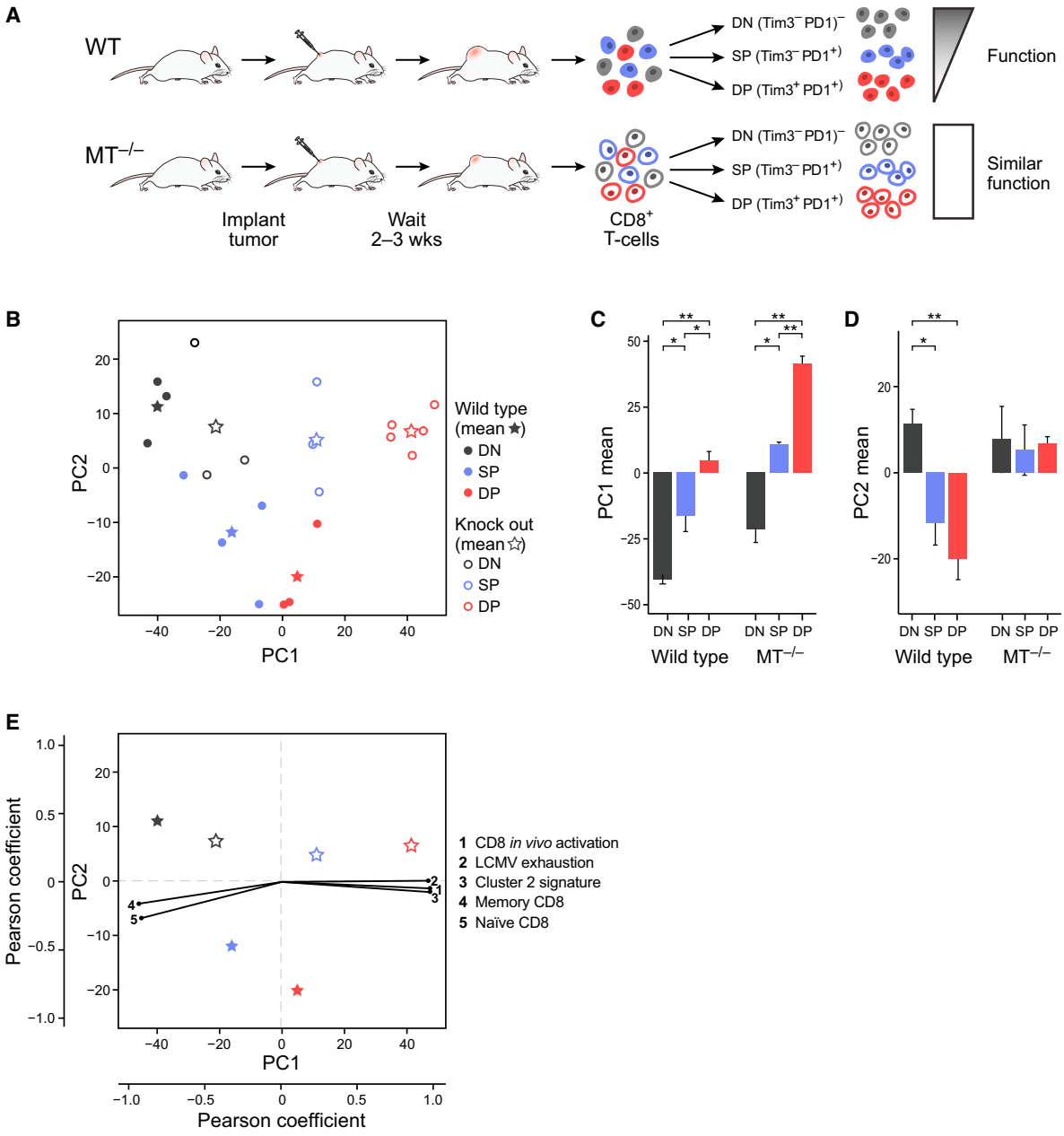

Figure 3. Transcriptional Profiling of *MT*$^{-/-}$ Enables Uncoupling of Activation and Dysfunction in CD8$^+$ TILs

(A) Outline of experimental strategy. B16F10 melanoma was used.

(B) PCA analysis of WT and *MT*$^{-/-}$ DN, SP, and DP TIL populations.

(C and D) Bar plots for the means of the PC1 (C) and PC2 (D) values for the DN, SP, and DP subpopulations. Error bars are the SEM estimator. p values for significance are computed using standard t test. *p < 0.05, **p < 0.01.

(E) Correlations of PC1 and PC2 values with various signatures. PC1 shows strong positive correlation with an in vivo CD8$^+$ activation signature (Sarkar et al., 2008), a CD8$^+$ viral exhaustion signature (Doering et al., 2012), and our cluster 2 gene signature (Figure 1B) and strong negative correlation with a naive CD8$^+$ and a memory CD8$^+$ signature (MSigDB [Subramanian et al., 2005], STAR Methods).

See also Figure S3 and Table S3.

signatures and memory CD8$^+$ T cell signatures (STAR Methods) (Eden et al., 2007; Wagner, 2015). Accordingly, we termed it a naive/memory-like module. The dysfunction module was enriched for a CD8$^+$ regulatory T cells (Treg) signature (Kim et al., 2015), suggesting that mechanisms present within the dysfunctional CD8$^+$ T cell population are shared with T cells that exhibit regulatory functions.

To test the relevance of our newly identified modules to human tumors, we compared our module scores to two signatures we recently obtained from CD8$^+$ TILs from melanoma patients by

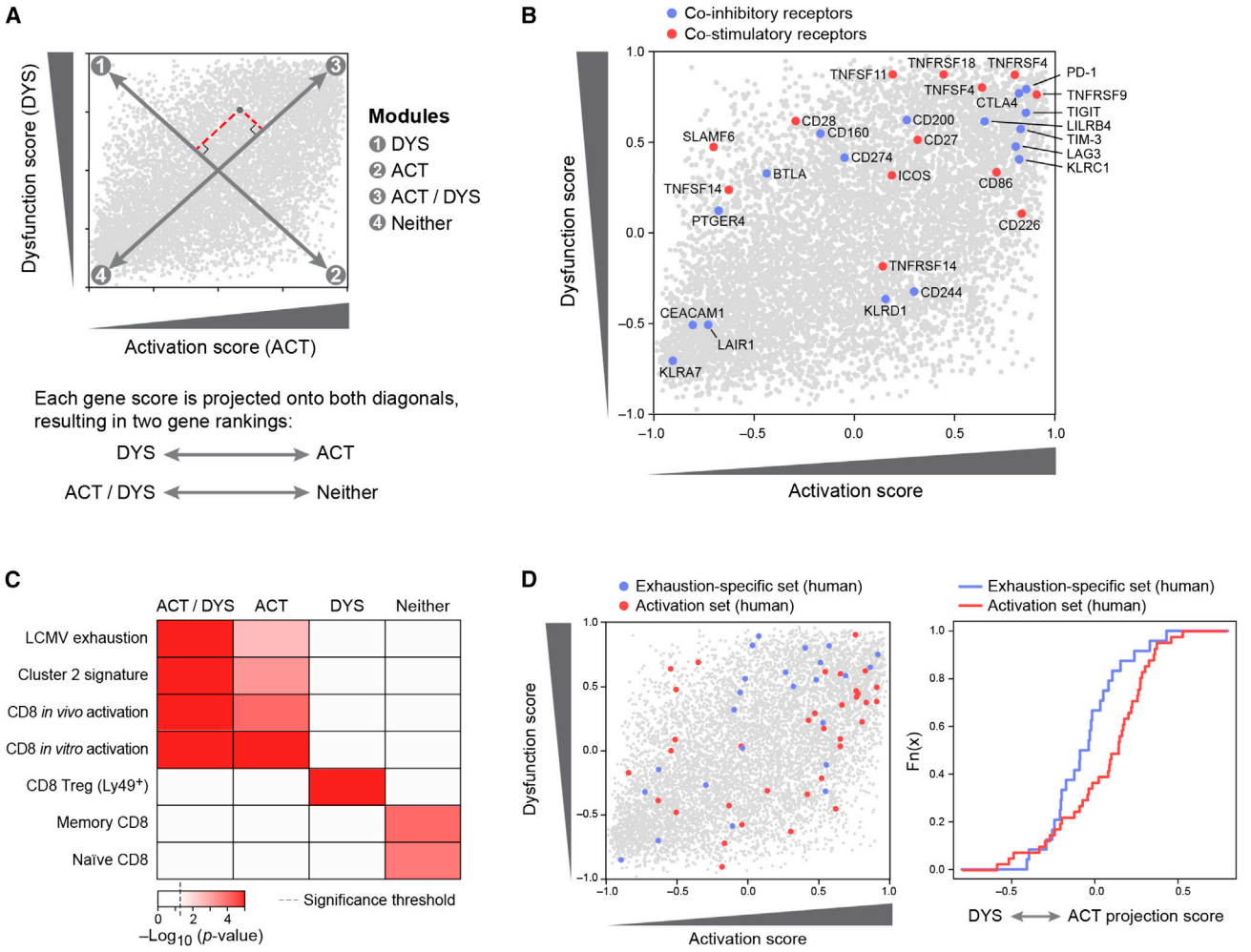

Figure 4. Identification of Gene Modules for T Cell Activation and Dysfunction

(A) Genes were projected onto both diagonal axes to determine a ranking of genes for their association with (1) dysfunction, (2) activation, (3) both dysfunction and activation, (4) neither.

(B) The distribution of genes by their dysfunction and activation scores reveals genes associated to different extents with the dysfunction and/or activation gene modules. Co-inhibitory receptors reported to be associated with both activation and dysfunction transcriptional profiles (e.g., PD-1, CTLA4, Tim3, Lag3) are seen in the upper-right corner.

(C) Enrichments of different signatures for the different modules of the activation/dysfunction plot. Dashed line marks p = 0.05 significance threshold.

(D) Genes from an exhaustion and activation signature defined in a human melanoma study (Tirosh et al., 2016) separate on the Dysfunction ↔ Activation axis we have defined (as shown in A). Shown is the distribution of genes on the Dysfunction/Activation plot (left) and the Kolmogorov-Smirnov plot of the values of the human signatures on the Dysfunction ↔ Activation axis (Axis 1–2 in A) (KS p = 0.027).

See also Table S4.

single-cell RNA-seq (Tirosh et al., 2016). In human melanoma TILs, we found evidence for a similar phenomenon with genes in the dysfunction module in human TILs having higher scores for the dysfunction module in our mouse TILs analysis compared to genes in the activation module ($p < 0.03$, Kolmogorov-Smirnov [KS] test, Figure 4D). Thus, the dysfunction module may be distinguishable in human TILs and may be clinically relevant.

The Dysfunction and Activation Gene Modules Are Uncoupled at the Single-Cell Level

The difference in transcriptional states of the bulk DN, SP, and DP populations between WT and $MT^{-/-}$ could stem from either changes in cell intrinsic states or from changes in the proportion of cells exhibiting different transcriptional states. To test whether the $CD8^+$ TILs in vivo include cells that express only the dysfunction module, but not the activation module, we analyzed 1,061 $CD8^+$ TILs with single-cell RNA-seq (516 WT and 545 $MT^{-/-}$ cells that passed QC thresholds from 1,504 processed cells) (STAR Methods). We then assigned each cell with "signature scores" based on the relative extent to which it expressed the different module signatures (while controlling for the cell's profile complexity, a measure of quality) (STAR Methods).

The activation and dysfunction module scores were negatively correlated across cells (Figure 5A), such that a higher

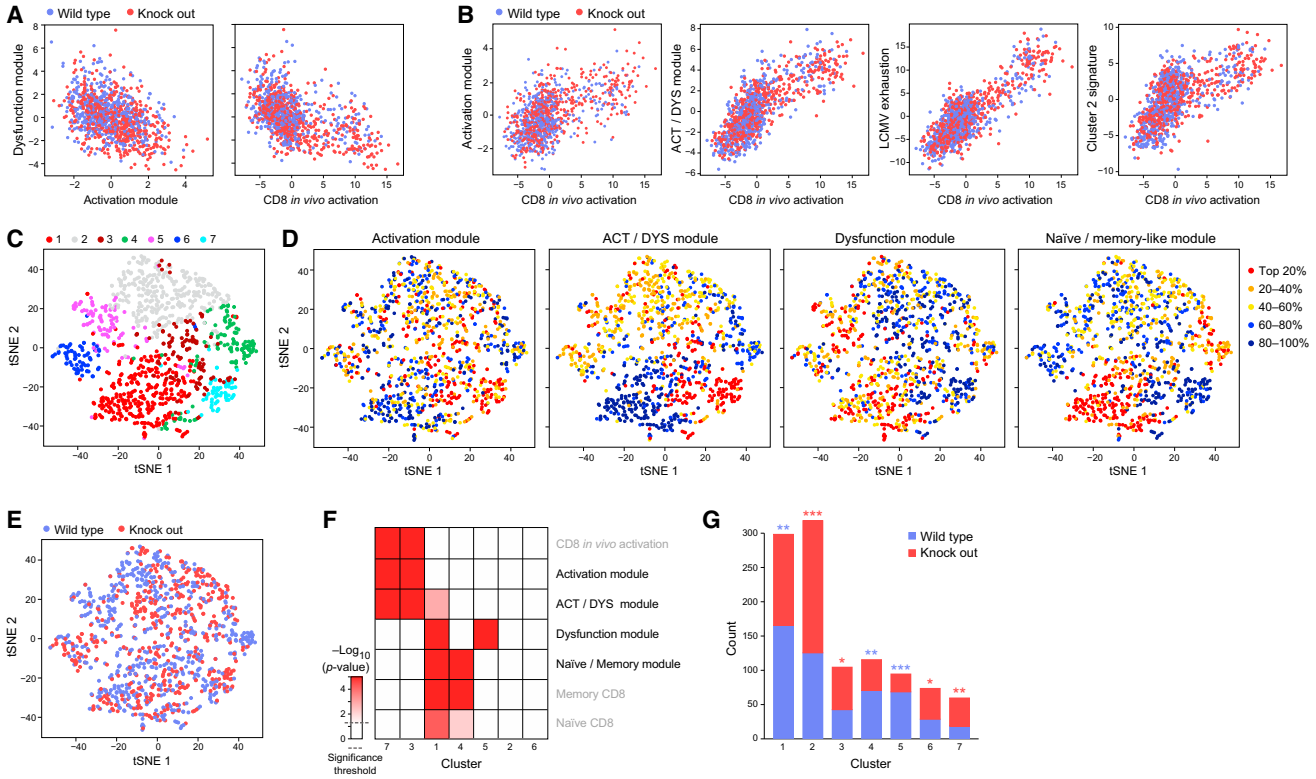

Figure 5. The Dysfunction and Activation Transcriptional Programs Are Negatively Correlated at the Single-Cell Level

(A) Expression of the dysfunction module at the single-cell level is negatively correlated with expression of the activation module (left, r = −0.42) and of an in vivo CD8$^+$ activation signature (Sarkar et al., 2008) (right, r = −0.47).

(B) Expression of an in vivo CD8$^+$ activation signature at the single-cell level is positively correlated with expression of (left to right) the activation module (r = 0.57), the activation/dysfunction module (r = 0.79), a viral LCMV exhaustion signature (r = 0.85), and the cluster 2 genes (Figure 1B) (r = 0.68).

(C–E) A tSNE visualization (van der Maaten and Hinton, 2008) of the 1,061 single-cells analyzed, colored by (C) the partitioning into seven clusters (infomap), (D) gene signatures of the four gene modules defined (by quantile), and (E) mouse type (WT or $MT^{-/-}$).

(F) Association of different gene signatures with the single-cell clusters (XL-mHG test, threshold at top 30% of list). Dashed line marks p = 0.05 significance threshold.

(G) Counts of cells from WT/$MT^{-/-}$ in the different clusters. Clusters significantly enriched for presence of WT (blue) or $MT^{-/-}$ cells (red) are marked. *p < 0.05, **p < 0.01, ***p < 0.001 (hypergeometric test).

See also Figure S4.

expression of one module's genes by a cell predicts lower expression of the other module's genes in the same cell. Similarly, the dysfunction module score was also negatively correlated with the in vivo CD8$^+$ activation signature (Sarkar et al., 2008). In contrast (Figure 5B), the expression of the in vivo CD8$^+$ activation signature (Sarkar et al., 2008) positively correlated with that of our annotated activation and activation/dysfunction signatures, as well as with the expression of a previously annotated signature of viral exhaustion (Doering et al., 2012) and our cluster 2 signature (Figure 1B). These observed trends were present in both the WT and $MT^{-/-}$ cells.

Next, unsupervised clustering of the CD8$^+$ TILs (using a k-nearest-neighbor graph followed by the Infomap clustering algorithm [Rosvall and Bergstrom, 2008] as previously described [Shekhar et al., 2016]; STAR Methods) partitioned the cells into seven clusters (visualized and colored in Figure 5C). Cluster 7 was enriched for cells with high levels of the activation module signature, whereas cluster 5 was enriched for cells with high expression of the dysfunction module signature (Figures 5D and 5F). Indeed, cells in cluster 7 had higher expression of perforin and several granzymes compared to those in cluster 5, suggesting better functional potential (Figure S4; $p < 10^{-8}$, Wilcoxon rank sum test). Consistent with these transcriptional signatures, cluster 5 is significantly enriched with cells from WT, where we observed T cell dysfunction, whereas cluster 7 is enriched for $MT^{-/-}$ TILs, in which there is improved effector function (Figures 5E and 5G). Thus, the dysfunction and activation transcriptional signatures are enriched in different cells and the presence of these modules in WT versus $MT^{-/-}$ CD8$^+$ TILs is aligned with the observed differences in their functional phenotypes. Furthermore, cells expressing the activation versus dysfunction modules can indeed be distinguished, and CD8$^+$ T cells indeed exist in vivo that express our computationally derived dysfunction module (Figure 4).

Gata-3 Regulates Dysfunction in CD8$^+$ TILs

To validate that members of the dysfunctional signature perform important functions and to identify candidate transcription factors (TFs) that may be critical for inducing T cell dysfunction independent of activation, we scored each TF that was consistently differentially expressed across our datasets for its rank in the four modules (Figures 5 and 6A). In the dysfunction module, Gata-3, a zinc-finger transcription factor, was the top-ranking transcription factor, followed by IKZF2, another zinc-finger TF, from a TF family known to regulate lymphocyte development (Kim et al., 2015), and then followed by SUDS3.

Several lines of evidence supported a role for Gata-3 in regulating CD8$^+$ TIL dysfunction. Genes bound by Gata-3 in nTregs are enriched in both the dysfunction ($p = 0.013$, hypergeometric test) and activation/dysfunction ($p = 0.0056$) module signatures; of the TFs consistently differentially expressed across our datasets, Gata3 is the top-ranking TF member of the dysfunction module (Figure 6A), and it is a member of cluster 2 (Figure 1B). We therefore hypothesized that Gata-3 may be involved, together with MT1 and MT2, in regulating CD8$^+$ T cell dysfunction. We analyzed Gata-3-expressing CD8$^+$ TILs from WT tumor-bearing mice and found that Gata-3 is expressed on a subpopulation of CD8$^+$ Tim3$^+$ TILs (Figure 6B), which upon stimulation expressed significantly lower levels of interferon-γ (IFN-γ) and IL-2, as well as significantly higher levels of IL-10 compared to Gata-3$^-$ CD8$^+$ TILs (Figure 6C). Thus, Gata-3$^+$ CD8$^+$ TILs are dysfunctional, producing low levels of pro-inflammatory cytokines and also actively producing the suppressive cytokine IL-10.

To directly test the role of Gata-3 in regulating CD8$^+$ T cell dysfunction, we knocked out Gata-3 in naive CD8$^+$ T cells using a lentivirus CRISPR-Cas9-targeting approach. We transduced single guide RNAs (sgRNAs), which were either non-targeting controls or targeted Gata-3, along with CRISPR-Cas9-expressing lentiviruses (STAR Methods) into CD8$^+$ T cells. We used PMEL transgenic mice in which all T cells have a single tumor-antigen-specific T cell receptor (TCR) with specificity for the mouse homolog of the human premelanosome protein. PMEL CD8$^+$ T cells are normally ineffective at controlling growth of B16F10 melanoma tumors, such that perturbations that promote tumor clearance can be readily discerned. We first determined the efficiency of Gata-3 deletion by quantitative real-time PCR (Figure 6D). Then, control or Gata-3-deleted PMEL CD8$^+$ T cells were activated, and equal numbers of cells were transferred into WT mice with established B16F10 melanoma tumor. Mice were then followed for tumor growth. Transfer of Gata-3-deleted PMEL CD8$^+$ T cells significantly delayed tumor growth (Figure 6E). Furthermore, similar to *MT*$^{-/-}$ CD8$^+$ T cells, the loss of Gata-3 in CD8$^+$ T cells did not alter the expression of Tim-3 and PD-1 on CD8$^+$ TILs (Figure 6F), but it improved CD8$^+$ T cell function with increased frequency of IFN-γ^+ and IL-2$^+$ cells (Figure 6G). Taken together, these data support a role for Gata-3 as a regulator of T cell dysfunction.

CONCLUSIONS

Here, we combined computational, molecular, and functional systems immunology to derive a distinct signature for T cell dysfunction that is uncoupled from T cell activation. Although chronic activation is a pre-requisite to T cell dysfunction, our data show that these two T cell states are separable transcriptionally and genetically. Single-cell RNA-seq of TILs supports our observation that T cells with either state exist in vivo. Importantly, the dysfunction and activation gene modules are consistent with signatures in CD8$^+$ TILs in human melanoma (Tirosh et al., 2016), supporting their clinical relevance. The ability to dampen the dysfunction gene module while not interfering with the activation gene module of a T cell is highly desirable in the setting of cancer or chronic viral infection. In contrast, the ability to effectively engage the dysfunction gene module while dampening the activation gene module is desirable in the setting of autoimmunity.

We find that the expression of co-inhibitory receptors can be uncoupled from dysfunctional phenotype. Indeed, many co-inhibitory receptors are not in the dysfunction module but, rather, are in the activation/dysfunction gene module. Thus, while co-inhibitory receptors may set the stage for the development of T cell dysfunction, eventually chronic engagement of the TCR and co-inhibitory receptors must drive the cells to initiate a distinct gene program for T cell dysfunction. It will be interesting to see how a co-inhibitory receptor blockade alters the expression of the activation, dysfunction, and activation/dysfunction modules in cells.

The uncoupling of the dysfunction module from the activation module does not in itself determine any obvious relationship between the two modules or how they might be expressed in cells. Our single-cell analysis of TILs revealed that, not only are the two modules negatively correlated with each other, but they also can be exclusively enriched in distinct populations of CD8$^+$ T cells. These findings suggest that, while dysfunctional T cells may have arisen from activated T cells, they acquire a distinct functional state with a transcriptional program that is no longer dependent on the activation module. Nevertheless, the fact that we observe enrichment for the activation and dysfunction modules in different cells in our single-cell analysis does not mean that our newly defined modules cannot be expressed in the same cells. How these modules are expressed in individual cells will best be discerned by examining cells throughout a time course of tumor development. Such a study will shed light on potential transitional T cell states.

Our data point to zinc regulation by metallothioneins and the function of zinc-dependent transcription factors as key features that lead to the development of the dysfunctional T cell phenotype. Interestingly, MT1 and MT2 are among the differentially expressed genes found in a signature of dysfunctional T cells from chronic LCMV viral infection (Doering et al., 2012), as are several zinc-finger-containing transcription factors. These observations support a role for metallothioneins and zinc regulation in determining effector CD8$^+$ T cell phenotype and that zinc dysregulation may be at the core of the dysfunctional phenotype across multiple chronic disease conditions. Indeed, zinc is an essential metal required for the structure and function of more than 1,000 zinc-finger-containing proteins that include several families of transcription factors (GATA, IKAROS, nuclear hormone receptors, Kruppel-like factors), RING-domain ubiquitin ligases, serine-threonine kinases, and matrix metallopeptidases. Thus,

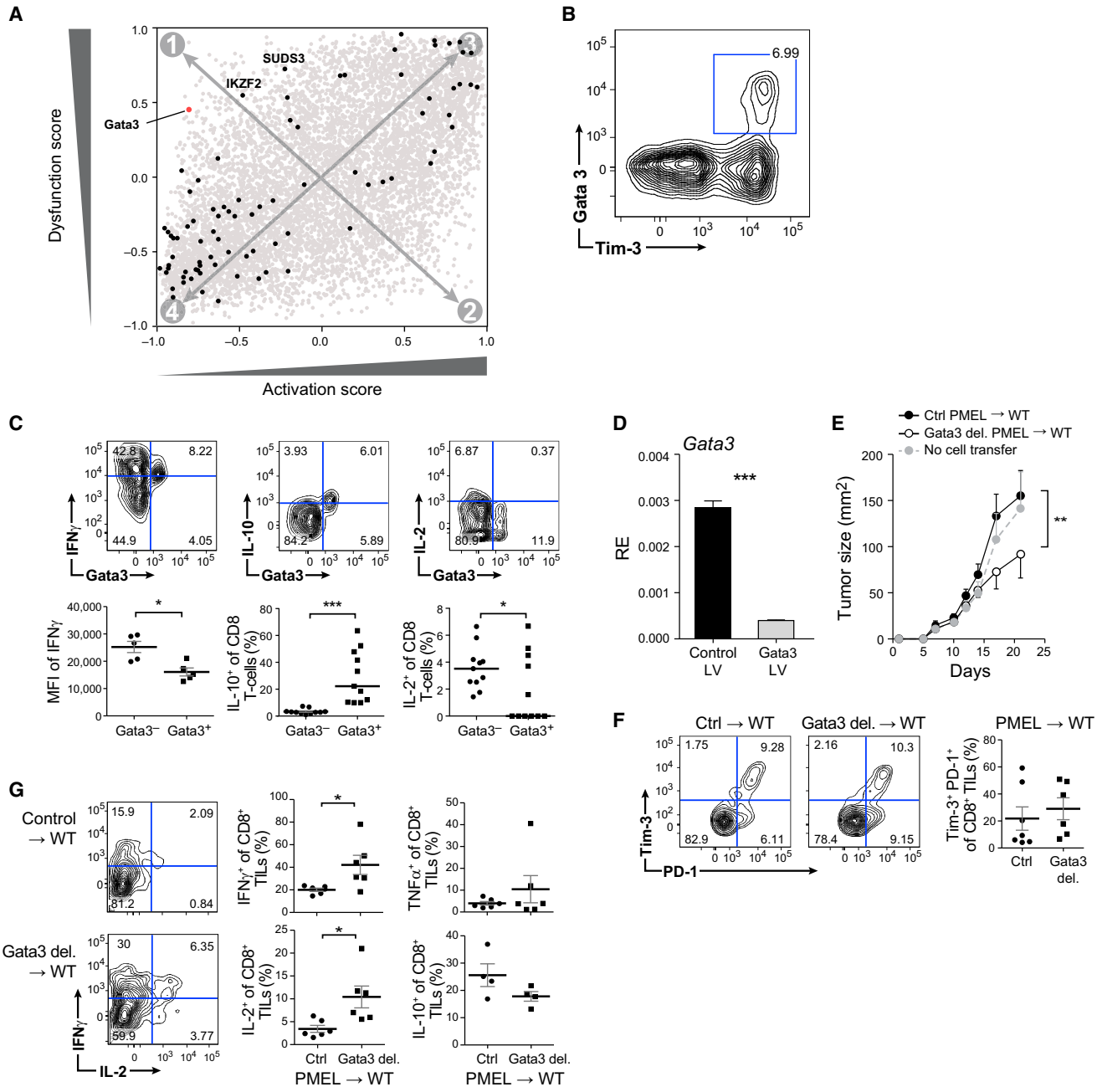

Figure 6. Gata3 Drives the Dysfunctional State in CD8⁺ T Cells

(A) Gata3, a zinc-binding TF, ranks first in the dysfunction module of the TFs consistently differentially expressed across our datasets (black points).

(B and C) WT mice were implanted subcutaneously with B16F10 melanoma cells. TILs were isolated on day 15 and analyzed for Gata3 expression and T cell function. (B) Representative flow cytometry data showing Gata3 expression gated on CD8⁺ TILs. (C) Cytokine expression of Gata3⁺ and Gata3⁻ CD8⁺ TILs. Statistical analysis was performed using paired Student's *t* test. *p < 0.05, ***p < 0.001.

(D) Targeted deletion of Gata3 using CRISPR-Cas9 genome editing. Naive CD8⁺ T cells were sorted from pmel transgenic mice, infected with control or Gata3 lentivirus, and activated with plate-bound anti-CD3 and anti-CD28 antibodies in the presence of IL-2 (STAR Methods). Representative qPCR results showing Gata3 mRNA level in control versus Gata3 lentivirus-targeted CD8⁺ T cells.

(E) 1 × 10^6 CRISPR-Cas9-targeted cells were transferred to WT mice (n = 5/group) bearing B16F10 melanoma tumors (day 5 post tumor grafting). Mean tumor growth is shown. Data are representative of three independent experiments. Statistical analysis was performed using linear regression. **p < 0.01.

(F and G) TILs were isolated on day 21 after tumor cell injection and analyzed for Tim-3 and PD-1 expression (F) and cytokine production (G) by flow cytometry.

one can envision how disruption of intracellular zinc availability can impact the structure and activity of multiple proteins that regulate cellular functions.

Consistent with this observation, our studies identify a novel role for the zinc-finger transcription factor Gata-3 as a driver of T cell dysfunction. Gata-3 has pleiotropic roles in immunity. While it is best known for promoting type 2 immune responses, Gata-3 has also been implicated in playing a role in T cell lineage development, development of ILC2s, controlling $CD8^+$ T cell proliferation, and more recently in regulatory T cell function (Tindemans et al., 2014). In the latter context, the role of Gata-3 in $CD8^+$ T cell dysfunction may reflect aspects of its role in promoting regulatory functions in T cells. Identification of other factors that co-operate with Gata-3 to drive the dysfunction program in $CD8^+$ T cells will pave the way for identification of the complete ensemble of transcriptional regulators that induce T cell dysfunction distinct from other functional or differentiation states in T cells.

Our newly identified dysfunction gene module shares some features with a recently identified signature for $Ly49^+$ $CD8^+$ T cells that have a regulatory phenotype (Kim et al., 2015) but not with the other annotated T cell signatures. Interestingly, the stability of this $Ly49^+$ $CD8^+$ Treg population is dependent on Helios (IKZF2), a zinc-finger of the IKAROS family, and the second-highest scoring TF (after Gata-3) of the TFs analyzed in our dysfunction gene module. Together, these data suggest that dysfunctional T cells may have adopted a regulatory program to curb their activity in the face of antigen persistence and chronic activation. Further annotation of genes in the dysfunction module identified through our single-cell analysis will shed light on the potential regulatory programs expressed by dysfunctional $CD8^+$ T cells.

Our findings refine our current definition of the dysfunctional T cell state by providing precise molecular resolution of the distinct gene programs associated with T cell dysfunction versus activation. The presence of our newly defined gene modules in T cells isolated from human melanoma tissue indicates the robustness of our findings and opens the door for the identification of novel "druggable" targets for the treatment of cancer and other chronic diseases.

STAR★METHODS

Detailed methods are provided in the online version of this paper and include the following:

SUPPLEMENTAL INFORMATION

Supplemental Information includes four figures and five tables and can be found with this article online at http://dx.doi.org/10.1016/j.cell.2016.08.052.

AUTHOR CONTRIBUTIONS

Conceptualization, M.S., C.W., V.K.K., A.R., and A.C.A.; Methodology, C.W., M.S., L.C., O.R.-R., A.R., V.K.K., and A.C.A.; Software, M.S., R.H.H., and H.Z.; Formal Analysis, M.S., C.W., H.Z., I.Y., and A.R.; Investigation, C.W., M.S., L.C., N.D.M., H.Z., and K.S.; Resources, S.K., J.N., D.G., M.S.K., R.H.H., J.X., J.Y.H.K., and J.N.; Writing, M.S., C.W., V.K.K., A.R., and A.C.A.; Supervision, A.C.A., A.R., V.K.K., and O.R.-R.; Funding Acquisition, V.K.K., A.R., and A.C.A.

ACKNOWLEDGMENTS

We thank Diane Mathis, Itay Tirosh, and Naomi Habib for fruitful discussions, Deneen Kozoriz for cell sorting, and Leslie Gaffney and Lior Friedman for help with artwork. This work was supported by grants from the NIH (R01NS045937 to V.K.K., P01AI073748 to V.K.K. and A.C.A., R01CA187975 to A.C.A., 5P01AI045757 to A.R.), the American Cancer Society (RSG-11-057-01-LIB to A.C.A.), by Koch Institute Support (core) grant P30-CA14051 from the National Cancer Institute and the Ludwig Center (to A.R.), and by the Klarman Cell Observatory at the Broad Institute and HHMI. A.R. is an Investigator of the Howard Hughes Medical Institute. C.W. was supported by an endMS Postdoctoral Fellowship from the Multiple Sclerosis Society of Canada. L.C. is a Cancer Research Institute Irvington Fellow supported by the Cancer Research Institute. M.S.K. was supported by Charles A. King Trust Postdoctoral Research Fellowship Program, Bank of America, N.A., Co-Trustee and the Simeon J. Fortin Charitable Foundation, Bank of America, N.A. A.C.A. is a member of the SAB for Potenza Therapeutics, Tizona Therapeutics, and Idera Pharmaceuticals, which have interests in cancer immunotherapy. V.K.K. has an ownership interest and is a member of the SAB for Potenza Therapeutics and Tizona Therapeutics. A.C.A.'s and V.K.K.'s interests were reviewed and managed by the Brigham and Women's Hospital and Partners Healthcare in accordance with their conflict of interest policies. A.R. is an SAB member for Thermo Fisher and Syros Pharmaceuticals and is a consultant for Driver Group. A provisional patent application was filed including work of this manuscript.

Received: July 14, 2016
Revised: August 14, 2016
Accepted: August 23, 2016
Published: September 8, 2016

REFERENCES

Anderson, A.C., Joller, N., and Kuchroo, V.K. (2016). Lag-3, Tim-3, and TIGIT: Co-inhibitory Receptors with Specialized Functions in Immune Regulation. Immunity *44*, 989–1004.

Baitsch, L., Baumgaertner, P., Devêvre, E., Raghav, S.K., Legat, A., Barba, L., Wieckowski, S., Bouzourene, H., Deplancke, B., Romero, P., et al. (2011). Exhaustion of tumor-specific $CD8^+$ T cells in metastases from melanoma patients. J. Clin. Invest. *121*, 2350–2360.

Baitsch, L., Fuertes-Marraco, S.A., Legat, A., Meyer, C., and Speiser, D.E. (2012). The three main stumbling blocks for anticancer T cells. Trends Immunol. *33*, 364–372.

Blackburn, S.D., Shin, H., Haining, W.N., Zou, T., Workman, C.J., Polley, A., Betts, M.R., Freeman, G.J., Vignali, D.A., and Wherry, E.J. (2009). Coregulation

of CD8+ T cell exhaustion by multiple inhibitory receptors during chronic viral infection. Nat. Immunol. *10*, 29–37.

Bonaventura, P., Benedetti, G., Albarède, F., and Miossec, P. (2015). Zinc and its role in immunity and inflammation. Autoimmun. Rev. *14*, 277–285.

Cong, L., Ran, F.A., Cox, D., Lin, S., Barretto, R., Habib, N., Hsu, P.D., Wu, X., Jiang, W., Marraffini, L.A., and Zhang, F. (2013). Multiplex genome engineering using CRISPR/Cas systems. Science *339*, 819–823.

Doering, T.A., Crawford, A., Angelosanto, J.M., Paley, M.A., Ziegler, C.G., and Wherry, E.J. (2012). Network analysis reveals centrally connected genes and pathways involved in CD8+ T cell exhaustion versus memory. Immunity *37*, 1130–1144.

Eden, E., Lipson, D., Yogev, S., and Yakhini, Z. (2007). Discovering motifs in ranked lists of DNA sequences. PLoS Comput. Biol. *3*, e39.

Fourcade, J., Sun, Z., Benallaoua, M., Guillaume, P., Luescher, I.F., Sander, C., Kirkwood, J.M., Kuchroo, V., and Zarour, H.M. (2010). Upregulation of Tim-3 and PD-1 expression is associated with tumor antigen-specific CD8+ T cell dysfunction in melanoma patients. J. Exp. Med. *207*, 2175–2186.

Fuertes Marraco, S.A., Neubert, N.J., Verdeil, G., and Speiser, D.E. (2015). Inhibitory Receptors Beyond T Cell Exhaustion. Front. Immunol. *6*, 310.

Gaublomme, J.T., Yosef, N., Lee, Y., Gertner, R.S., Yang, L.V., Wu, C., Pandolfi, P.P., Mak, T., Satija, R., Shalek, A.K., et al. (2015). Single-Cell Genomics Unveils Critical Regulators of Th17 Cell Pathogenicity. Cell *163*, 1400–1412.

Giordano, M., Henin, C., Maurizio, J., Imbratta, C., Bourdely, P., Buferne, M., Baitsch, L., Vanhille, L., Sieweke, M.H., Speiser, D.E., et al. (2015). Molecular profiling of CD8 T cells in autochthonous melanoma identifies Maf as driver of exhaustion. EMBO J. *34*, 2042–2058.

Hamer, D.H. (1986). Metallothionein. Annu. Rev. Biochem. *55*, 913–951.

Johnson, W.E., Li, C., and Rabinovic, A. (2007). Adjusting batch effects in microarray expression data using empirical Bayes methods. Biostatistics *8*, 118–127.

Kim, P.S., and Ahmed, R. (2010). Features of responding T cells in cancer and chronic infection. Curr. Opin. Immunol. *22*, 223–230.

Kim, H.J., Barnitz, R.A., Kreslavsky, T., Brown, F.D., Moffett, H., Lemieux, M.E., Kaygusuz, Y., Meissner, T., Holderried, T.A., Chan, S., et al. (2015). Stable inhibitory activity of regulatory T cells requires the transcription factor Helios. Science *350*, 334–339.

Langmead, B., Trapnell, C., Pop, M., and Salzberg, S.L. (2009). Ultrafast and memory-efficient alignment of short DNA sequences to the human genome. Genome Biol. *10*, R25.

Li, B., and Dewey, C.N. (2011). RSEM: accurate transcript quantification from RNA-Seq data with or without a reference genome. BMC Bioinformatics *12*, 323.

Matsuzaki, J., Gnjatic, S., Mhawech-Fauceglia, P., Beck, A., Miller, A., Tsuji, T., Eppolito, C., Qian, F., Lele, S., Shrikant, P., et al. (2010). Tumor-infiltrating NY-ESO-1-specific CD8+ T cells are negatively regulated by LAG-3 and PD-1 in human ovarian cancer. Proc. Natl. Acad. Sci. USA *107*, 7875–7880.

Picelli, S., Björklund, A.K., Faridani, O.R., Sagasser, S., Winberg, G., and Sandberg, R. (2013). Smart-seq2 for sensitive full-length transcriptome profiling in single cells. Nat. Methods *10*, 1096–1098.

Ran, F.A., Cong, L., Yan, W.X., Scott, D.A., Gootenberg, J.S., Kriz, A.J., Zetsche, B., Shalem, O., Wu, X., Makarova, K.S., et al. (2015). In vivo genome editing using Staphylococcus aureus Cas9. Nature *520*, 186–191.

Reich, M., Liefeld, T., Gould, J., Lerner, J., Tamayo, P., and Mesirov, J.P. (2006). GenePattern 2.0. Nat. Genet. *38*, 500–501.

Restifo, N.P., Smyth, M.J., and Snyder, A. (2016). Acquired resistance to immunotherapy and future challenges. Nat. Rev. Cancer *16*, 121–126.

Rosvall, M., and Bergstrom, C.T. (2008). Maps of random walks on complex networks reveal community structure. Proc. Natl. Acad. Sci. USA *105*, 1118–1123.

Sakuishi, K., Apetoh, L., Sullivan, J.M., Blazar, B.R., Kuchroo, V.K., and Anderson, A.C. (2010). Targeting Tim-3 and PD-1 pathways to reverse T cell exhaustion and restore anti-tumor immunity. J. Exp. Med. *207*, 2187–2194.

Sarkar, S., Kalia, V., Haining, W.N., Konieczny, B.T., Subramaniam, S., and Ahmed, R. (2008). Functional and genomic profiling of effector CD8 T cell subsets with distinct memory fates. J. Exp. Med. *205*, 625–640.

Shalek, A.K., Satija, R., Adiconis, X., Gertner, R.S., Gaublomme, J.T., Raychowdhury, R., Schwartz, S., Yosef, N., Malboeuf, C., Lu, D., et al. (2013). Single-cell transcriptomics reveals bimodality in expression and splicing in immune cells. Nature *498*, 236–240.

Shalem, O., Sanjana, N.E., Hartenian, E., Shi, X., Scott, D.A., Mikkelsen, T.S., Heckl, D., Ebert, B.L., Root, D.E., Doench, J.G., and Zhang, F. (2014). Genome-scale CRISPR-Cas9 knockout screening in human cells. Science *343*, 84–87.

Shekhar, K., Lapan, S.W., Whitney, I.E., Tran, N.M., Macosko, E.Z., Kowalczyk, M., Adiconis, X., Levin, J.Z., Nemesh, J., Goldman, M., et al. (2016). Comprehensive classification of retinal bipolar neurons by single-cell transcriptomics. Cell *166*, 1308–1323.

Subramanian, A., Tamayo, P., Mootha, V.K., Mukherjee, S., Ebert, B.L., Gillette, M.A., Paulovich, A., Pomeroy, S.L., Golub, T.R., Lander, E.S., and Mesirov, J.P. (2005). Gene set enrichment analysis: a knowledge-based approach for interpreting genome-wide expression profiles. Proc. Natl. Acad. Sci. USA *102*, 15545–15550.

Tindemans, I., Serafini, N., Di Santo, J.P., and Hendriks, R.W. (2014). GATA-3 function in innate and adaptive immunity. Immunity *41*, 191–206.

Tirosh, I., Izar, B., Prakadan, S.M., Wadsworth, M.H., 2nd, Treacy, D., Trombetta, J.J., Rotem, A., Rodman, C., Lian, C., Murphy, G., et al. (2016). Dissecting the multicellular ecosystem of metastatic melanoma by single-cell RNA-seq. Science *352*, 189–196.

van der Maaten, L., and Hinton, G. (2008). Visualizing data using t-SNE. J. Mach. Learn. Res. *9*, 26.

Wagner, F. (2015). GO-PCA: an unsupervised method to explore gene expression data using prior knowledge. PLoS ONE *10*, e0143196.

Wherry, E.J., and Kurachi, M. (2015). Molecular and cellular insights into T cell exhaustion. Nat. Rev. Immunol. *15*, 486–499.

Wherry, E.J., Ha, S.J., Kaech, S.M., Haining, W.N., Sarkar, S., Kalia, V., Subramaniam, S., Blattman, J.N., Barber, D.L., and Ahmed, R. (2007). Molecular signature of CD8+ T cell exhaustion during chronic viral infection. Immunity *27*, 670–684.

Zhou, Q., Munger, M.E., Veenstra, R.G., Weigel, B.J., Hirashima, M., Munn, D.H., Murphy, W.J., Azuma, M., Anderson, A.C., Kuchroo, V.K., and Blazar, B.R. (2011). Coexpression of Tim-3 and PD-1 identifies a CD8+ T-cell exhaustion phenotype in mice with disseminated acute myelogenous leukemia. Blood *117*, 4501–4510.

Zuniga, E.I., Macal, M., Lewis, G.M., and Harker, J.A. (2015). Innate and adaptive immune regulation during chronic viral infections. Annu. Rev. Virol. *2*, 573–597.

STAR★METHODS

KEY RESOURCES TABLE

REAGENT or RESOURCE	SOURCE	IDENTIFIER
Antibodies		
Rat anti-PD-1 (clone: RMP1-30)	Biolegend	Cat#109109; RRID: AB_572016
Anti-Tim3 (clone: 5D12)	Generated in house	N/A
Rat anti-IL-2 (clone: JES6-5H4)	Biolegend	Cat#503807; RRID: AB_315301
Anti-TNF-α (clone: MP6-XT22)	eBioscience	Cat#117321; RRID: AB_10670212
Anti-IFN-γ (clone: XMG-1.2)	Biolegend	Cat#505829; RRID: AB_10897937
Mouse anti-Granzyme B (clone: GB11)	Biolegend	Cat#515405; RRID: AB_515405
Rat anti-CD8 (clone: 53-6.7)	Biolegend	Cat#100731; RRID: AB_893427
Chemicals, Peptides, and Recombinant Proteins		
Zinpyr-1	Santa Cruz	Cat#sc-213182
Fixable viability dye eFluor506	eBioscience	Cat#65-0866
Gp100	Genscript	Cat#RP20344
Critical Commercial Assays		
High Sensitivity DNA Kit (Bioanalyzer)	Agilent	Cat#5067-4626
Qubit dsDNA, High Sensitivity 500rxn	Thermo Fisher Scientific	Cat#Q32854
Nextera XT Sample Preparation Kit	Illumina	Cat#FC-131-1096
NextSeq 500 high output kit V2, 75 cycles	Illumina	Cat#FC-404-2005
Deposited Data		
Data files for $CD8^+$ populations, Microarray	This paper	GEO: GSE86042
Data files for bulk RNA sequencing	This paper	GEO: GSE86042
Data files for single-cell RNA sequencing	This paper	GEO: GSE86042
LCMV exhaustion signature	Doering et al., 2012	GEO: GSE41867
$CD8^+$ $Ly49^+$Treg signature	Kim et al., 2015	GEO: GSE73015
Experimental Models: Cell Lines		
MC38-OVA	Mark Smyth	N/A
CT26	ATCC	Cat#CRL-2638; RRID: CVCL_7256
B16-F10	ATCC	Cat#CRL-6475; RRID: CVCL_0159
Experimental Models: Organisms/Strains		
Balb/c	Jackson Laboratory	Cat#000651; RRID: IMSR_JAX:000651
C57BL/6	Jackson Laboratory	Cat#000664; RRID: IMSR_JAX:000664
PMEL	Jackson Laboratory	Cat#005023; RRID: MMRRC_005023-UCD
OTI	Jackson Laboratory	Cat#003831; RRID: MMRRC_003831-UCD
$MT^{-/-}$ (backcrossed to C57BL/6 in house)	Jackson Laboratory	Cat#002211; RRID: IMSR_JAX:002211
Recombinant DNA		
SMARTER TSO (with LNA, 10 μM))	Exiqon	5′-AAGCAGTGGTATCAACGCAGAGTACrGrG+G-3′
PCR oligonucleotide primer (10 μM)	IDT	5′-AAGCAGTGGTATCAACGCAGAGT-3′
Reverse Transcription DNA oligonucleotide primer (RNase-free, 100 μM)	IDT	5′-AAGCAGTGGTATCAACGCAGAGTACT(30)VN-3′
Sequence-Based Reagents		
Gata3 CRISPR guide sequence	Designed in house	5′ - GGTATCCTCCGACCCACCACG

(*Continued on next page*)

Continued

REAGENT or RESOURCE	SOURCE	IDENTIFIER
Software and Algorithms		
GenePattern	Reich et al., 2006	http://software.broadinstitute.org/cancer/software/genepattern/
COMBAT	Johnson et al., 2007	http://www.bu.edu/jlab/wp-assets/ComBat/Download.html
Bowtie	Langmead et al., 2009	http://bowtie-bio.sourceforge.net/index.shtml
RSEM	Li and Dewey, 2011	http://deweylab.github.io/RSEM/
XL-mHG	Wagner, 2015	https://github.com/flo-compbio/xlmhg

CONTACT FOR REAGENT AND RESOURCE SHARING

Requests of reagents should be directed to Ana C. Anderson at acanderson@partners.org.

EXPERIMENTAL MODEL AND SUBJECT DETAILS

Mice

6–8 week old female Balb/c, C57BL/6, pMEL, and OTI transgenic mice were purchased from the Jackson Laboratory. Mice deficient in metallothionein 1 and 2 ($MT^{-/-}$) were purchased from the Jackson Laboratory and backcrossed onto the C57BL/6 background for 5 generations and were confirmed to be > 97% congenic with C57BL/6 by SNP analysis. All mice were housed under SPF conditions. All experiments involving laboratory animals were performed under protocols approved by the Harvard Medical Area Standing Committee on Animals (Boston, MA).

Tumor Experiments

CT26 and B16F10 were purchased from ATCC. MC38-Ova was generously provided by Mark Smyth. CT26 and MC38-Ova ($1x10^6$) or B16F10 ($5x10^5$) were implanted subcutaneously into the right flank. Tumor size was measured in two dimensions by caliper and is expressed as the product of two perpendicular diameters. For adoptive transfer tumor experiments, naive ($CD8^+CD62L^+CD44^{lo}$) T cells from PMEL (for CRISPR-Cas9 targeting experiments) or OT-1 (for overexpression of MT) transgenic mice were isolated by cell sorting (BDFACS Aria) and activated by 2ug/ml each of plate-bound anti-CD3 and anti-CD28 antibodies for 48 hr, rested for 3 days, and then reactivated with 1ug/ml of anti-CD3 and antiCD28 antibodies for 2 days prior to transfer into recipient mice. Retroviral and lentiviral infections of primary T cells were optimized and experiments were performed as described in the respective figure legends. Briefly, retrovirus was used to spin-infect T cells one day after activation and lentivirus was used to infect T cells twice, at 16 hr prior to activation and at 4 hr post activation. Targeting efficiency of retrovirus was determined by measuring GFP expression in both control and MT overexpressing cultures; whereas effective CRISPR-Cas9-mediated deletion of the target gene using lentivirus was determined by qPCR.

METHOD DETAILS

Isolation and Analysis of TILs

TILs were isolated by dissociating tumor tissue in the presence of collagenase D (2.5 mg/ml) for 20 min prior to centrifugation on a discontinuous Percoll gradient (GE Healthcare). Isolated cells were then used in various assays of T cell function. Cells were cultured in DMEM supplemented with 10% (vol/vol) FCS, 50 μM 2-mercaptoethanol, 1 mM sodium pyruvate, nonessential amino acids, L-glutamine and 100 U/ml penicillin and 100 μg/ml streptomycin.

Flow Cytometry

Single cell suspensions were stained with antibodies against surface molecules. CD4 (RM4-5), CD8 (53-6.7), and PD-1 (RMP1-30) antibodies are purchased from BioLegend. Tim-3 (5D12) antibody was generated in house. Fixable viability dye eF506 (eBioscience) was used to exclude dead cells. For intra-cytoplasmic cytokine staining, cells were stimulated with 12-myristate 13-acetate (PMA) (50ng/ml, Sigma-Aldrich, MO), ionomycin (1μg/ml, Sigma-Aldrich, MO) in the presence of Brefeldin A (Golgiplug, BD Bioscience) for four hours prior to staining with antibodies against surface proteins followed by fixation and permeabilization and staining with antibodies against IL-2 (JES6-5H4), TNF-α (MP6-XT22) (eBioscience), IFN-γ (XMG-1.2), and Granzyme B (GB11) (Biolegend). For measurement of intracellular zinc, cells were stained with 1 μM Zinpyr-1 (Santa Cruz) in PBS for 20 min at 37deg, washed with media, followed by regular surface staining. All data were collected on a BD LsrII (BD Biosciences) and analyzed with FlowJo software (Tree Star).

Proliferation Assays

Tumor draining lymph nodes and tumor infiltrating lymphocytes were harvested and incubated with or without tumor specific antigen (gp100, 5 μM) for four consecutive days and cell proliferation was measured by ^3H incorporation assay.

Generation of Lentiviral Constructs and CRISPR-Cas9 Targeting

The initial guide sequences were selected based on the exon structure of target genes and ranked by the repertoire of potential off-target sites to select designs that minimize the possibility of off-target cleavage. The guides were then cloned into CRISPR-Cas9 vectors via golden-gate cloning as described previously (Cong et al., 2013). The final guide sequence selected for Gata3 is: 5′ – GGTATCCTCCGACCCACCACG. The vector used is a lenti-viral vector, pCKO_2, bearing mammalian-codon-optimized SaCas9 linked to puromycin selection cassette (Ran et al., 2015; Shalem et al., 2014), and an sgRNA-expression cassette that has been modified to enhance RNA expression. The constructs were sequence verified and then tested to screen for the efficiency of each guide using a mouse T-lymphocyte cell line, EL4 (ATCC) before moving on to lentiviral production. To quantify the genomic modification induced by the CRISPR-Cas9 system, genomic DNA was extracted using QuickExtract Solution (Epicenter), as described previously (Cong et al., 2013). Indel formation was measured by either SURVEYOR nuclease assay (IDT DNA) or targeted deep sequencing as described previously (Cong et al., 2013). Briefly, the genomic region around the CRISPR-Cas9 targeting site was amplified, and then subject to either SURVEYOR nuclease digestion following re-annealing or re-amplified to add on Illumina P5/P7 adapters with barcodes for deep-sequencing analysis using the MiSeq sequencing system (Illumina).

After screening of guides in cell lines, the top-ranked guides based on their targeting efficiency were used for viral production. 293FT cells (Thermo Fisher) were maintained as recommended by the manufacturer in 150mm plates. For each transfection, 10 μg of pVSVG envelope plasmid, 15 μg of pDelta packaging plasmids, and 20 μg of pCKO_2 vector carrying the construct of interest were used. The transfection was either carried out using lipofectamine 2000 (Thermo Fisher) following the manufacturer's recommendations, or with PEI, where 5:1 ratio of PEI solution was added to the DNA mixture, and incubated for 5 min before adding the final complex onto cells. After incubation for 16 hr, 20 ml of fresh warm media was applied to replace the old growth media. Virus was harvested between 48h and 72h post transfection by taking the supernatant and pelleting cell debris via centrifugation. The viral particles were then filtered through a 0.45 μm filtration system (Millipore), and then either directly used as purified supernatant, or concentrated further with 15 ml Amicon concentrator (Millipore). Lentiviral vectors were titered by real-time qPCR using a customized probe against the transgene.

For all primary T cell experiments, the efficacy of the CRISPR-Cas9 lentiviral vectors was first tested by transducing in vitro primary mouse T cell culture, followed by cleavage measurement and qPCR detection of target gene knock-down. The most efficient viral constructs were then used for downstream experiments.

RNA Processing

Microarray Processing and Analysis

Samples consisting of naive ($CD62L^{hi}CD44^{low}$) and effector/memory ($CD62L^{low}CD44^{hi}$) $CD8^+$ cells from non-tumor-bearing Balb/c mice, $CD8^+Tim3^-PD1^-$ (DN) TILs, $CD8^+Tim3^-PD1^+$(SP), and $CD8^+Tim3^+PD1^+$ (DP) TILs were loaded on Affymetrix GeneChip Mouse Genome 430 2.0 Arrays.

Individual.CEL files were RMA normalized and merged to an expression matrix using the ExpressionFileCreator of GenePattern with default parameters (Reich et al., 2006). COMBAT (Johnson et al., 2007) was used to correct for batch effects (samples were generated in three batches), and probe intensity values below 20 or above 20,000 were collapsed to 20 and 20,000, respectively. Gene-specific intensities were then computed by taking for each gene *j* and sample *i* the maximal probe value observed for that gene: $y_{ij} = \max(p_i \mid \text{s.t. } p_i \text{ in set\_probes\_gene\_}j)$, and samples were transferred to log-space by taking $\log_2$(intensity). Differentially expressed genes were annotated as genes with either (1) an FDR-corrected ANOVA p-value smaller or equal to 0.01 computed across the DN, SP and DP subpopulations and a fold-change of at least 1.3 between any of the three subpopulations, or (2) a fold-change of at least 2 between any of the three subpopulations. Fold-change between each two subpopulations was computed as the minimum between the fold-changes of the medians and the means of the subpopulation samples. A differential-expression rank was computed for each gene as the mean between the gene's ranking based on its ANOVA p-value and its ranking based on fold-change. Clusters of differentially expressed genes were generated by *k*-means clustering (Hartigan-Wong algorithm, run in R) to 10 clusters of the scaled median values of the five sample types clustered over: DN, SP, DP, EffMem and naive CD8. Enrichment analysis for each cluster with MSigDB v5.0 (Subramanian et al., 2005) gene sets was computed as the hypergeometric p-value for the overlap between the cluster and the gene set of interest, out of the differentially expressed gene list. *P*-values for enrichment were FDR-corrected.

Population RNA-Seq Processing and Normalization

We profiled RNA from DP, SP, and DN from four WT and five $MT^{-/-}$ male mice in two batches (batch #1: 2 WT, 2 $MT^{-/-}$, batch #2: 2 WT, 3 $MT^{-/-}$). Samples were processed with SMART-Seq2 (Picelli et al., 2013), reads were aligned to the mouse mm9 transcriptome using Bowtie (Langmead et al., 2009), and expression abundance TPM estimates were obtained using RSEM parameters (Li and Dewey, 2011). Three samples were excluded from further analysis due to poor sequencing quality, and three additional samples were excluded due to being strong outliers on the first three principle components of the initial PCA (generated as described in next section; a trend similar to PC2 of Figure 3B, but not significant, was observed on PC4 prior to the latter sample exclusion). Each gene of each sample was assigned the value of $\log_2$(TPM+1). COMBAT (Johnson et al., 2007) was used to correct for batch effects, and was followed by Quantile Normalization to account for variability in library sizes.

To profile the RNA of in vitro activated $CD8^+$ T cells, we isolated naive $CD8^+$ cells from non-tumor-bearing C57BL/6 mice and activated them with anti-CD3 and anti-CD28 in vitro. Samples were processed with the SMART-Seq2 protocol (Picelli et al., 2013), mapped to mm9 with Bowtie (Langmead et al., 2009) and TPM values were computed by RSEM (Li and Dewey, 2011).

Single-Cell RNA-Seq

For single-cell RNA-Seq experiments, TILs from B16 melanomas were collected in 96-well plates, incorporating a population-well and an empty well in each plate as controls, and were processed from the four WT mice (two plates per mouse; total of eight WT plates) and five $MT^{-/-}$ mice (one plate each from two of the mice ($MT^{-/-}$ 1,2) and two plates each from three of the mice ($MT^{-/-}$ 4,5,6)); total of eight $MT^{-/-}$ plates). Samples were produced in 2 biological batches (batch #1: WT1,2, $MT^{-/-}$ 1,2,3, batch #2: WT3,4, $MT^{-/-}$ 4,5,6), and processed in 4 sequencing batches, where each sequencing batch consisted of two WT plates and two $MT^{-/-}$ plates.

Cells were sorted into 96-well plates with 5 μl lysis buffer comprised of Buffer TCL (QIAGEN 1031576) plus 1% 2-mercaptoethanol (Sigma 63689). Following sorting, plates were spun down for one minute at 3,000 rpm and immediately frozen at −80°C. For preparation of single-cell libraries we thawed the cells and purified them with 2.2x RNAClean SPRI beads (Beckman Coulter Genomics) without final elution (Shalek et al., 2013). The RNA captured beads were air-dried and processed immediately for cDNA synthesis. We performed SMART-seq2 following the published protocol (Picelli et al., 2013) with minor modifications in the reverse transcription (RT) step (MSK and AR, in preparation). We made a 25μl reaction mix for each PCR and performed 21 cycles for cDNA amplification. We used 0.25ng cDNA of each cell and one-fourth of the standard Illumina NexteraXT reaction volume in both the tagmentation and final PCR amplification steps. We pooled plates to 384 single-cell libraries, and sequenced 50 × 25 paired-end reads using a single kit on the NextSeq500 5 instrument.

QUANTIFICATION AND STATISTICAL ANALYSIS

Population RNA-Seq Analysis

Principal Component Analysis

PCA was run on the centered expression matrix (as obtained in the previous section) of the 4,155 genes with mean expression ≥ 3 and a fold-change of at least 1.5 between at least one pair of samples. To investigate the association of the PCs with $CD8^+$ T cell activation, the profiles from naive and in vitro stimulated $CD8^+$ T cells were quantile-normalized together with the samples by which the PCA was produced (above), and overlaid onto the PCA (following subtraction of the gene-specific values used for centering of the PCA-generating dataset).

Computing a Dysfunction and Activation Score and the Annotation of Dysfunction and Activation Related Gene Modules and Gene Signatures

Each gene was assigned an ''activation score'' defined as the correlation of the gene's expression across the samples with the PC1 values, computed over the MTKO samples. Additionally, each gene was assigned a ''dysfunction score'' to be (−1) times the correlation of the gene's expression across the samples with the PC2 values, computed over the WT samples. These two scores placed the gene on the Activation / Dysfunction plot as shown in Figure 4A. We included in this analysis the 7,592 genes that had an assigned $\log_2$(TPM+1) expression value ≥ 4, in at least two of the samples. Following placement on the Activation / Dysfunction plot, each gene was assigned two rankings: on the Dysfunction ↔ Activation axis, and on the Activation ⟍ Dysfunction ↔ Neither axis, by projecting each point onto the x = (-y) and x = y axes, respectively. We defined four rankings of the 7,592 genes, each ranking representing the association of these genes with one of the following: (1) dysfunction (and not activation): by the (−1)*x values of the x = (-y) projection (ranking from the Dysfunction corner to the Activation corner), (2) activation (and not dysfunction): by the x values of the x = (-y) projection (3) activation and dysfunction: by the x values of the x = y projection, and (4) neither: by the (−1)*x values of the x = y projection.

To check for statistically significant association of different expression signatures with these four rankings (dysfunction / activation / activation ⟍ dysfunction / neither) we used the XL-mHG test (Eden et al., 2007; Wagner, 2015) to test for enrichment at the tops of the different ranked lists (one test for each module), requiring that the minimal number of genes in an enriched set to be 5 (X = 5) and that the proportion of the ranked list to be considered in the enrichment portion be at most 30% of the list (L = 30%). Our reported significance results are robust to a variety of XL-mHG parameters, including the completely unconstrained ranked test (X = 0; L = 100%).

From each of the four rankings, we annotated a gene signature of 100 genes, defining gene signatures for: (1) dysfunction (and not activation), (2) activation (and not dysfunction), (3) activation and dysfunction; and (4) neither. Each signature was defined to be the top-most ranked genes of the relevant ranking, which fulfilled the following constraints: all genes included in the Dysfunction signature had a dysfunction score of ≥ 0.3, all genes included in the Activation signature had an activation score of ≥ 0.3 and all genes included in the Activation/Dysfunction signature had activation and dysfunction scores ≥ 0.3.

Single-Cell RNA-Seq Analysis

Paired reads were mapped to mouse annotation mm10 using Bowtie (Langmead et al., 2009) (allowing a maximum of one mismatch in seed alignment, and suppressing reads that had more than 10 valid alignments), TPMs were computed using RSEM (Li and Dewey, 2011), and $\log_2$(TPM+1) values were used for subsequent analyses.

We filtered out low quality cells and cell doublets, maintaining for subsequent analysis the 1,061 cells (516 WT and 545 $MT^{-/-}$) that had (1) 1,500-6,000 detected genes (defined by at least one mapped read), (2) at least 100,000 reads mapped to the transcriptome, and (3) at least 20% of the reads mapped to the transcriptome. We restricted the genes considered in subsequent analyses to be the 9,863 genes expressed at $\log_2(TPM+1) \geq 2$ in at least twenty of the cells.

PCA of the Gene-by-Cell matrix revealed PC1 to be highly correlated with the cells' gene-counts (Gaublomme et al., 2015), and it was therefore excluded from subsequent analyses to reduce technical bias. We chose PCs 2-7 for subsequent analysis due to a drop in the proportion of variance explained following PC7. To visualize cell-to-cell variation we used tSNE (van der Maaten and Hinton, 2008) to generate a two-dimensional non-linear embedding.

To obtain clusters of cells similar in their expression patterns, cells were clustered using the infomap algorithm (Rosvall and Bergstrom, 2008) which was ran on the binary k-nearest-neighbor graph, where k = 70 (Shekhar et al., 2016).

P-values for enrichment of each cluster with a given gene signature were computed by ranking the cells by their cell-specific-gene-signature-scores (see below), and computing the XL-mHG test (X = 5; L = 30% of ranked cell list) to generate a p value for the enrichment of cells from the given cluster at the top of the ranked list.

Single-Cell Gene Signature Scoring

As an initial step, genes were binned into six bins based on their mean expression across cells, and into six (separate) bins based on their variance of expression across cells. Given a gene signature (list of genes), a cell-specific signature score was computed for each cell as follows: First, 1,000 random gene lists were generated, where each instance of a random gene-list was generated by sampling (with replacement) for each gene in the gene-list a gene that is equivalent to it with respect to the mean and variance bins it was placed in. Then, the sum of gene expression in the given cell was computed for all gene-lists (given the 1,000 random lists generated) and the z-score of the original gene-list for the generated 1,000 sample distribution is returned. For gene-signatures consisting of an upregulated and downregulated set of genes, two z-scores were obtained separately, and the downregulated associated z-score was subtracted from the upregulated generated z-score.

Generation of Gene Signatures from the Literature

For the $CD8^+$ in vivo activation signature, we used the intersection of the sets of genes published in Sarkar et al. (Sarkar et al., 2008) as (1) DE between effector and naive, (2) DE between effector and memory.

For the LCMV exhaustion (viral exhaustion) signature, we identified differentially expressed genes between the acute and chronic conditions for each time point in (Doering et al., 2012), as genes significantly different under an FDR-corrected t test ($p < 0.05$) and that had a fold-change in expression ≥ 2. The exhaustion set was taken as the union of the Day 15 DE genes and the Day 30 DE genes.

For the $CD8^+$ $Ly49^+$Treg signature, gene expression measurements for Ly49+ and Ly49- $CD8^+$ T cells (two replicates each) were downloaded from GEO: GSE73015 (Kim et al., 2015). Differentially expressed genes were determined as genes with (1) a mean fold-change ≥ 1.5 and (2) a fold-change ≥ 1.3 between the smallest sample from the upregulated condition and the largest sample of the downregulated condition.

For the in vitro activation signature, differentially expressed genes were determined as genes with (1) a mean fold-change ≥ 2 and (2) a fold-change ≥ 1.3 between the smallest sample from the upregulated condition and the largest sample of the downregulated condition.

For the naive $CD8^+$ T cell signature, a signature was compiled from 26 MSigDB (v5.0, c7) (Subramanian et al., 2005) gene signatures identified as upregulated in naive $CD8^+$ T cells when compared to effector, memory, or exhausted $CD8^+$ T cells at various time points (Table S5). The 28 genes present in at least 10 of the analyzed sets were selected for this signature.

For the memory $CD8^+$ T cell signature, we compiled 13 MSigDB (v5.0, c7) (Subramanian et al., 2005) gene signatures identified as upregulated in memory $CD8^+$ T cells when compared to naive, effector or exhausted $CD8^+$ T cells at various time points (Table S5). The 23 genes present in at least 6 of the analyzed sets were selected for this signature.

DATA AND SOFTWARE AVAILABILITY

Data Resources

The data generated in this paper has been deposited in the Gene Expression Omnibus (GEO) under accession number GEO: GSE86042.

Integrated and normalized expression measurements of naive, effector/memory and TILs subpopulations: Table S1.

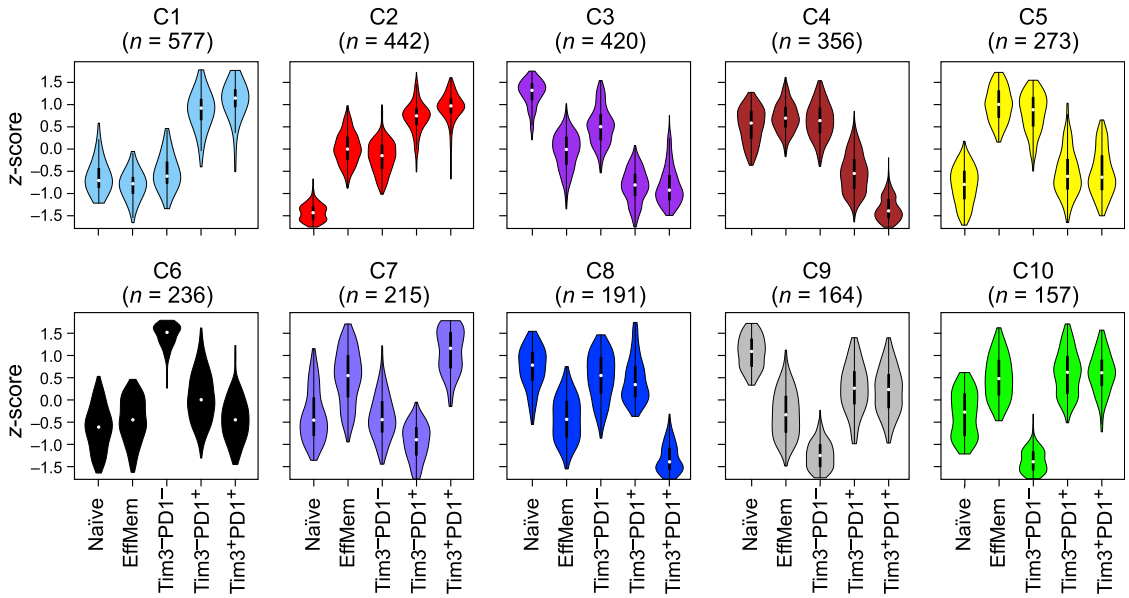

Figure S1. Expression Trends of CD8⁺ TILs Clusters, Related to Figure 1

Each of the ten clusters obtained (see Figure 1B) had a different expression trend across the five subpopulations. See Table S1 for expression values and cluster assignments of genes and Table S2 for MSigDB enrichments of the different clusters.

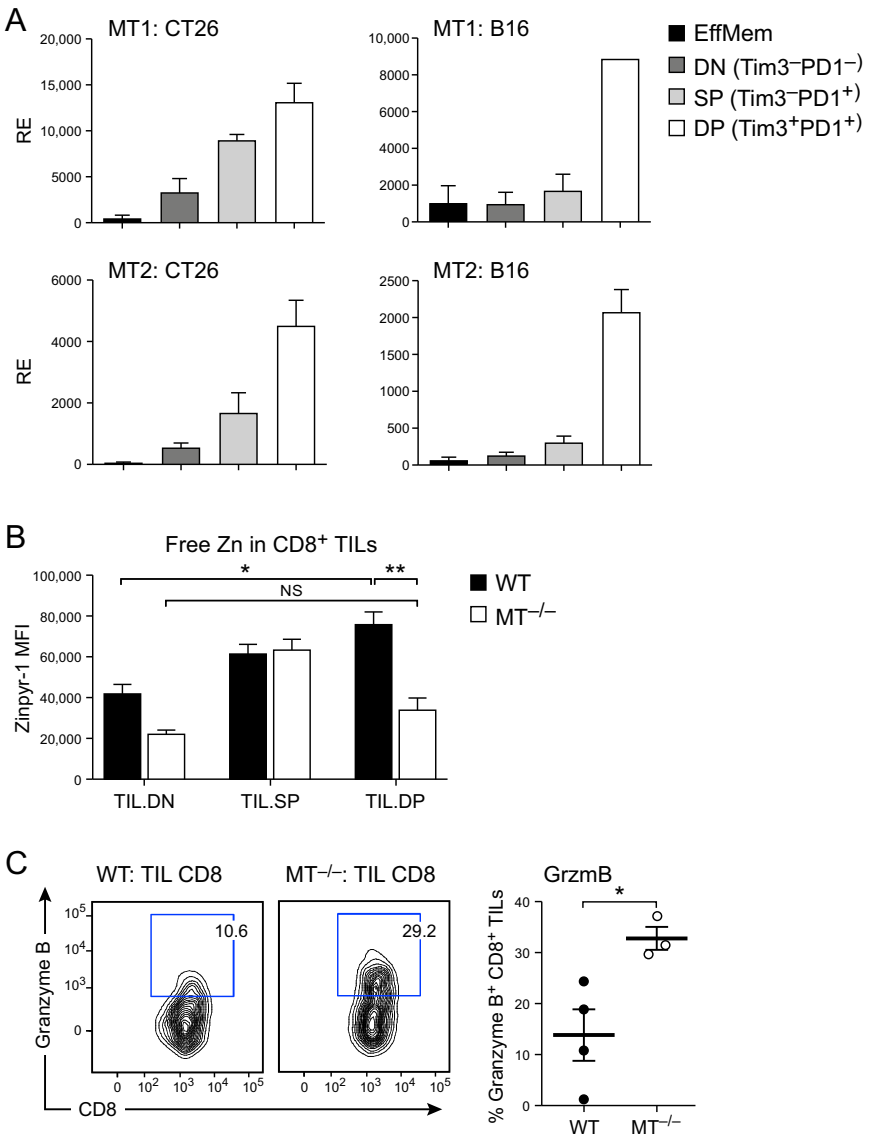

Figure S2. Metallothionein Expression, Zinc Dysregulation, and Effector Function in CD8$^+$ TILs, Related to Figure 2

(A) Expression of MT1 and MT2 as determined by qPCR in sorted CD8$^+$ TILs isolated from mice bearing CT26 colon carcinoma and B16 melanoma tumors. (B) WT and *MT*$^{-/-}$ TILs were stained with Zinpyr-1 for measuring free Zn followed by cell surface staining and analyzed by flow cytometry. C) Granzyme expression in WT and *MT*$^{-/-}$ CD8$^+$ TILs.

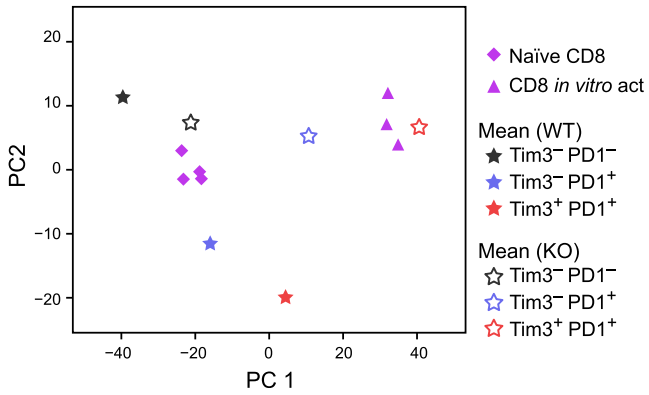

Figure S3. Overlay of Naive and In Vitro Activated CD8$^+$ T Cell Transcriptomes on PC1 and PC2, Related to Figure 3

Naive CD8$^+$CD62L^{hi}CD44^{low} were isolated from C57BL/6 mice by cell sorting and stimulated in vitro with plate bound anti-CD3/anti-CD28. On day 3, cells were harvested and following RNA sequencing where overlaid onto the PCA plot generated from the DN, SP and DP subpopulations of WT and *MT*$^{-/-}$ TILs (STAR Methods).

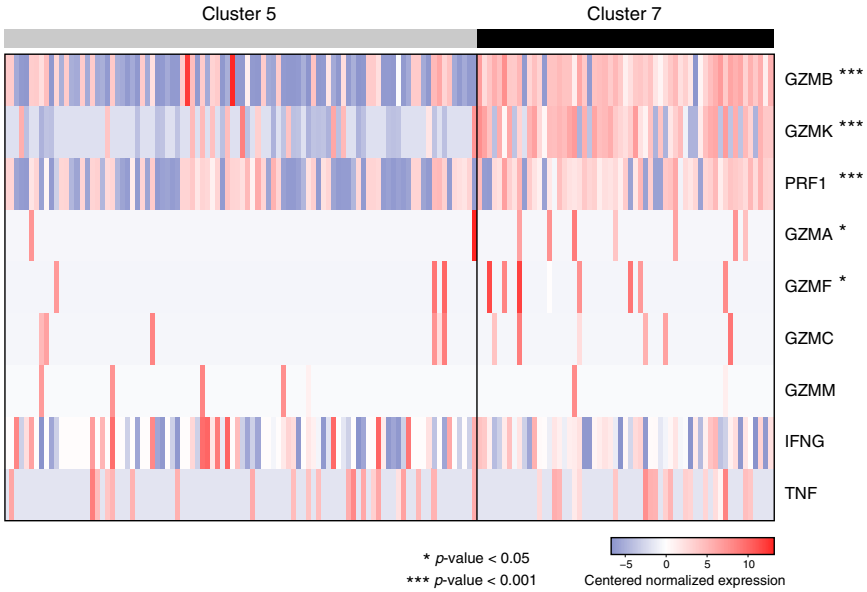

Figure S4. Cytokine and Effector Molecule Expression in Single-Cell Clusters 7 and 5, Related to Figure 5

Centered and normalized RNA levels are shown for different cytokines or effector molecules (rows) for each of the cells (columns) in clusters 5 and 7 from the single-cell analysis of Figure 5. To correct for differences in library complexity between cells and allow a comparison at the single-gene level, expression levels for all genes and cells analyzed (Figure 5) were normalized by partitioning cells into 10 bins by their library complexity and conducting a median-normalization procedure for each gene, as previously described (Gaublomme et al., 2015). IL2, GZMD and GZME are not included in this analysis because they did not pass the required expression thresholds to be included in the overall single-cell analysis (STAR Methods). *p < 0.05, ***p < 0.001. Overall p value for cytokine/effector molecule signature was $p < 10^{-8}$, (Wilcoxon rank sum test).